

# Cosmology with Phase Statistics: Parameter Forecasts and Detectability of BAO

Alexander Eggemeier,<sup>1\*</sup> and Robert E. Smith<sup>1</sup>

<sup>1</sup>*Astronomy Centre, University of Sussex, Falmer, Brighton, BN1 9QH, UK*

Accepted XXX. Received YYY; in original form ZZZ

## ABSTRACT

We consider an alternative to conventional three-point statistics such as the bispectrum, which is purely based on the Fourier phases of the density field: the line correlation function. This statistic directly probes the non-linear clustering regime and contains information highly complementary to that contained in the power spectrum. In this work, we determine, for the first time, its potential to constrain cosmological parameters and detect baryon acoustic oscillations (hereafter BAOs). We show how to compute the line correlation function for a discrete sampled set of tracers that follow a local Lagrangian biasing scheme and demonstrate how it breaks the degeneracy between the amplitude of density fluctuations and the bias parameters of the model. We then derive analytic expressions for its covariance and show that it can be written as a sum of a Gaussian piece plus non-Gaussian corrections. We compare our predictions with a large ensemble of  $N$ -body simulations and confirm that BAOs do indeed modulate the signal of the line correlation function for scales 50–100  $h^{-1}$ Mpc, and that the characteristic S-shape feature would be detectable in upcoming Stage IV surveys at the level of  $\sim 4\sigma$ . We then focus on the cosmological information content and compute Fisher forecasts for an idealized Stage III galaxy redshift survey of volume  $V \sim 10 h^{-3} \text{Gpc}^3$  and out to  $z = 1$ . We show that, combining the line correlation function with the galaxy power spectrum and a Planck-like microwave background survey, yields improvements up to a factor of two for parameters such as  $\sigma_8$ ,  $b_1$  and  $b_2$ , compared to using only the two-point information alone.

**Key words:** Cosmology: theory, Large-scale structure of Universe, Methods: analytical, Methods: numerical

## 1 INTRODUCTION

The clustering of galaxies in our Universe is commonly analyzed with one of the two simple statistical measures: the two-point correlation function or its Fourier space analogue, the power spectrum. Measurements of these statistics in the last decade led to the astonishing detection of baryon acoustic oscillations (hereafter BAO) in the clustering pattern of galaxies (Eisenstein et al. 2005; Tegmark et al. 2006) and subsequently to the increasingly precise constraints on our cosmological models which have confirmed the accelerated expansion rate of the present day Universe (see e.g. Alam et al. 2016, for a combination of two-point measurements from the final BOSS data release).

Over the next decades, further improvements are expected through developing theoretical advances that will enable us to extract information from deeper in the non-linear

regime and through surveying larger volumes of space and so beating down the sample variance errors. However, the former is very challenging, especially as the scales involved approach shell crossing and the realm of uncertain baryonic physics effects takes hold, while the latter will come to a halt once surveys approach the cosmic variance limit. The path forward thus inevitably turns the question: what else should we measure to improve our understanding of the Universe? Higher-order statistics such as the three-point function, or equivalently the bispectrum, are obvious answers. For several decades the advantages of these measures have been known: the configuration dependence of the bispectrum allows us to break degeneracies present in the power spectrum, making it efficient in constraining galaxy bias (Fry 1994; Matarrese et al. 1997); it was also shown to place improved constraints on other cosmological parameters (Sefusatti et al. 2006). Unfortunately, a wider application of these measures has been impeded by the slow development of improved theoretical modelling of these statistics and the

\* E-mail: a.eggemeier@sussex.ac.uk

challenge of accurate covariance matrices, which require very large sets of mock galaxy catalogues (see [Gil-Marín et al. 2016](#); [Slepian et al. 2016](#), for recent measurements of three-point statistics, though). For that reason a number of simpler statistics have been proposed, which only measure a subset of the available three-point information and are designed to constrain certain parameters. These are for instance the bias estimators defined in [Pollack et al. \(2014\)](#) and [Schmittfull et al. \(2015\)](#) as well as the position dependent power spectrum ([Chiang et al. 2014](#)) and the related skew-spectra ([Munshi & Heavens 2010](#)), which measure squeezed limits of higher-order statistics. Another idea that aims to compress bispectrum information into only a small number of modes was first explored in [Regan et al. \(2012\)](#).

In this paper, we follow yet a different approach. As the power spectrum depends only on the squared amplitude of the Fourier mode, it is insensitive to the phase of the mode. Consequently, a measure purely based on these phases will strictly probe information that is not already contained in the power spectrum ([Watts et al. 2003](#)). Provided the density field is Gaussian, the phases remain random and a complete statistical description can be given in terms of the power spectrum. After initial perturbations start growing under the influence of gravity, though, correlations among the phases emerge, indicating a flow of information into higher-order moments of the density field. Phase information is therefore a direct probe of the non-linear regime and an appropriate measure for non-Gaussian information in the density field.

One phase based statistic that has emerged in recent times is the ‘line correlation function’ (LCF) [Obreschkow et al. \(2013\)](#). It is defined as the three-point correlation function of the phases of the density field, whose three points are equally spaced on a line, each separated by a scale  $r$ . In [Obreschkow et al. \(2013\)](#) and [Eggemeier et al. \(2015\)](#) it was shown that the LCF provides a useful measure for quantifying the cosmic web, being able to differentiate between elongated, filamentary structures and node like structures (see also [Alpaslan et al. 2014](#)). [Obreschkow et al. \(2013\)](#) also showed that the LCF could be used to differentiate between cold and warm dark matter scenarios. [Wolstenhulme et al. \(2015\)](#) revealed the LCF’s relation to conventional statistical quantities and showed that, at lowest order in standard perturbation theory (hereafter SPT), it can be expressed as a combination of bispectrum and power spectra, but that it in principle should contain information from cumulants of even higher order. Several further developments were made by [Eggemeier et al. \(2015\)](#), among which was the quantification of the effects of redshift space distortions on the LCF.

Even though the LCF is closely related to the bispectrum, it should be expected to exhibit different dependencies on cosmological parameters and also different covariance properties. Furthermore, it offers the possibility to measure in principle even higher-order information with just a three-point function. All that makes the LCF an interesting alternative to the standard methods, which is worth investigating more closely. This paper thus aims to understand the response of the LCF to variations in the underlying cosmological models and to quantify the signal-to-noise of the estimates. Coupling together these quantities we aim to assess the cosmological parameter sensitivity of the LCF for upcoming galaxy redshift surveys that can be broadly classed

as Stage III and Stage IV, in the language of the Dark Energy Task Force ([Albrecht et al. 2006](#)).

The paper is broke down as follows: in §2 we provide a brief review of the LCF, we show how to compute the galaxy LCF and develop an analytic derivation of its covariance matrix. These theoretical predictions are then confronted with measurements from a large ensemble of N-body simulations in Sec. 4, before we move on to discuss the parameter sensitivity and error forecasts in Sec. 6, supported by a number of N-body simulations with varying cosmologies. Sec. 7 finally gives our conclusions.

## 2 PREDICTIONS FROM THEORY

### 2.1 The matter line correlation function

Consider a large volume of space within which is the realisation of a statistical homogeneous and isotropic random field. For a given scale  $r$ , the LCF of matter fluctuations can be defined as (for details see [Obreschkow et al. 2013](#); [Wolstenhulme et al. 2015](#)):

$$\ell_m(r) \equiv V^3 \left( \frac{r^3}{V} \right)^{3/2} \left\langle \epsilon_r(\mathbf{x}) \epsilon_r(\mathbf{x} + \mathbf{r}) \epsilon_r(\mathbf{x} - \mathbf{r}) \right\rangle \quad (1)$$

where the first factor is a volume regularisation term, with  $V$  being the volume of the survey and  $\epsilon_r(\mathbf{x})$  is the real space phase field smoothed on scale  $r$ . The Fourier transform of the smoothed phase field can be written:

$$\epsilon_r(\mathbf{x}) = \int \frac{d^3\mathbf{k}}{(2\pi)^3} \epsilon_{\mathbf{k}} e^{i\mathbf{k}\cdot\mathbf{x}} W(k|r) \quad (2)$$

where the window function is a spherical top-hat in  $k$ -space:  $W(k|r) = \Theta(1 - kr/2\pi)$  and with  $\Theta(x)$  being the Heaviside function. The phase field can now be readily defined as  $\epsilon(\mathbf{k}) \equiv \delta(\mathbf{k})/|\delta(\mathbf{k})|$ , with  $\delta(\mathbf{k})$  being the Fourier transform of the overdensity field. Note that the angle brackets in Eq. (1) indicate an averaging over an ensemble of random fields. Under the assumption of Ergodicity of the fields this becomes an average over volume and orientation of the direction vector of the line  $\hat{\mathbf{r}}$  at each point in space.

On substitution of Eq. (2) into Eq. (1) we find that the line correlation can also be written:

$$\begin{aligned} \ell_m(r) = & \frac{V^3}{(2\pi)^9} \left( \frac{r^3}{V} \right)^{3/2} \iiint_{|\mathbf{k}_1|, |\mathbf{k}_2|, |\mathbf{k}_3| \leq 2\pi/r} d^3\mathbf{k}_1 d^3\mathbf{k}_2 d^3\mathbf{k}_3 \\ & \times \left\langle \epsilon_{\mathbf{k}_1} \epsilon_{\mathbf{k}_2} \epsilon_{\mathbf{k}_3} \right\rangle \int \frac{d\hat{\mathbf{r}}}{4\pi} e^{i[\mathbf{k}_1 \cdot \mathbf{x} + \mathbf{k}_2 \cdot (\mathbf{x} + \mathbf{r}) + \mathbf{k}_3 \cdot (\mathbf{x} - \mathbf{r})]}, \end{aligned} \quad (3)$$

with the solid angle element  $d\hat{\mathbf{r}} \equiv \sin\vartheta d\vartheta d\varphi$ . In order to proceed further one has to compute the ensemble average of the three phase factors,

$$\langle \epsilon_{\mathbf{k}_1} \epsilon_{\mathbf{k}_2} \epsilon_{\mathbf{k}_3} \rangle = \langle \exp[i(\theta_{\mathbf{k}_1} + \theta_{\mathbf{k}_2} + \theta_{\mathbf{k}_3})] \rangle. \quad (4)$$

This expression can be evaluated by means of the joint probability density function (PDF) of Fourier phases,  $\mathcal{P}(\{\theta_{\mathbf{k}}\})$ , which was derived in [Matsubara \(2003, 2006\)](#). As is detailed in App. A, for weakly non-Gaussian fields the PDF can be expanded in an Edgeworth series of higher order correlators (in Fourier space poly-spectra) and using this result, one

finds that to lowest order (Wolstenhulme et al. 2015):

$$\langle \epsilon_{\mathbf{k}_1} \epsilon_{\mathbf{k}_2} \epsilon_{\mathbf{k}_3} \rangle \approx \frac{(2\pi)^3}{V} \left( \frac{\sqrt{\pi}}{2} \right)^3 \frac{B(\mathbf{k}_1, \mathbf{k}_2, \mathbf{k}_3)}{\sqrt{V P(\mathbf{k}_1) P(\mathbf{k}_2) P(\mathbf{k}_3)}} \times \delta_D(\mathbf{k}_1 + \mathbf{k}_2 + \mathbf{k}_3). \quad (5)$$

where the Dirac delta function  $\delta_D$  appears in the above expression as a consequence of statistical homogeneity of the phase field, and where  $P$  and  $B$  are the power spectrum and bispectrum of the matter field, respectively. These are defined:

$$\langle \delta_{\mathbf{k}} \delta_{\mathbf{k}'} \rangle \equiv (2\pi)^3 \delta_D(\mathbf{k} + \mathbf{k}') P(\mathbf{k}); \quad (6)$$

$$\langle \delta_{\mathbf{k}_1} \delta_{\mathbf{k}_2} \delta_{\mathbf{k}_3} \rangle \equiv (2\pi)^3 \delta_D(\mathbf{k}_1 + \mathbf{k}_2 + \mathbf{k}_3) B(\mathbf{k}_1, \mathbf{k}_2, \mathbf{k}_3). \quad (7)$$

The explicit dependence of Eq. (5) on the volume and hence the suppression of phase correlations in bigger surveys might appear surprising. However, with increasing volume the density field will contain a greater number of halos and thus peaks in density. As has been shown in Hikage et al. (2004), the more peaks of comparable heights are enclosed in the sampling volume, the more the distribution of the phase sum will approach a uniform value. If this distribution becomes uniform, phase correlations are consequently diluted.

Finally on inserting Eq. (5) into Eq. (3) and integrating over  $\mathbf{k}_1$  we find that at leading order, the line correlation can be written as an integral of the form:

$$\ell_m(r) \approx r^{9/2} \left( \frac{\sqrt{\pi}}{2} \right)^3 \iint_{|\mathbf{k}_1|, |\mathbf{k}_2|, |\mathbf{k}_1 + \mathbf{k}_2| \leq 2\pi/r} \frac{d^3 \mathbf{k}_1}{(2\pi)^3} \frac{d^3 \mathbf{k}_2}{(2\pi)^3} \times \frac{B(\mathbf{k}_1, \mathbf{k}_2, \mathbf{k}_1 + \mathbf{k}_2)}{\sqrt{P(\mathbf{k}_1) P(\mathbf{k}_2) P(\mathbf{k}_1 + \mathbf{k}_2)}} \int \frac{d\hat{\mathbf{r}}}{4\pi} e^{i(\mathbf{k}_1 - \mathbf{k}_2) \cdot \mathbf{r}}, \quad (8)$$

where after computing the integral we made the following relabelings  $\mathbf{k}_2 \rightarrow \mathbf{k}_1$  and  $\mathbf{k}_3 \rightarrow \mathbf{k}_2$ . Finally, on computing the average over all orientations of  $\mathbf{r}$  we arrive at the result:

$$\ell_m(r) \simeq \left( \frac{r}{4\pi} \right)^{9/2} \iint_{|\mathbf{k}_1|, |\mathbf{k}_2|, |\mathbf{k}_1 + \mathbf{k}_2| \leq 2\pi/r} d^3 \mathbf{k}_1 d^3 \mathbf{k}_2 \times \frac{B(\mathbf{k}_1, \mathbf{k}_2, \mathbf{k}_1 + \mathbf{k}_2)}{\sqrt{P(\mathbf{k}_1) P(\mathbf{k}_2) P(\mathbf{k}_1 + \mathbf{k}_2)}} j_0(|\mathbf{k}_1 - \mathbf{k}_2| r), \quad (9)$$

where  $j_0(x) = \sin x/x$  is the zeroth order spherical Bessel function.

## 2.2 LCF from standard perturbation theory

On applying nonlinear SPT to the fluid equations for primordial Gaussian matter fluctuations in an expanding universe, one finds that at lowest order (tree-level) the bispectrum can be expressed in terms of the linear power spectrum  $P$  and a mode coupling kernel  $F_2$  as (Fry 1984; Bernardeau et al. 2002):

$$B(\mathbf{k}_1, \mathbf{k}_2, \mathbf{k}_3) = 2 F_2(\mathbf{k}_1, \mathbf{k}_2) P_1 P_2 + \text{cyc.}, \quad (10)$$

where in the above and in what follows we will use the shorthand notation  $P_i \equiv P(k_i)$  and  $P_{ij} \equiv P(|\mathbf{k}_i - \mathbf{k}_j|)$  and the power spectra are understood to be those obtained from linear theory. The mode coupling kernel  $F_2$  reads:

$$F_2(\mathbf{k}_1, \mathbf{k}_2) = \frac{5}{7} + \frac{\hat{\mathbf{k}}_1 \cdot \hat{\mathbf{k}}_2}{2} \left( \frac{k_1}{k_2} + \frac{k_2}{k_1} \right) + \frac{2}{7} \left( \hat{\mathbf{k}}_1 \cdot \hat{\mathbf{k}}_2 \right)^2, \quad (11)$$

dropping its very weak dependence on the cosmological parameters (Bernardeau et al. 2002). On using again Eq. (5) and inserting Eq. (10) in this expression one can now choose to perform the integrations over the Dirac delta function so that the matter LCF at tree level can be expressed as (Wolstenhulme et al. 2015):

$$\ell_m(r) = 2 \left( \frac{r}{4\pi} \right)^{9/2} \iint_{|\mathbf{k}_1|, |\mathbf{k}_2|, |\mathbf{k}_1 + \mathbf{k}_2| \leq 2\pi/r} d^3 \mathbf{k}_1 d^3 \mathbf{k}_2 F_2(\mathbf{k}_1, \mathbf{k}_2) \times \sqrt{\frac{P_1 P_2}{P_{12}}} \left[ j_0(|\mathbf{k}_2 - \mathbf{k}_1| r) + 2j_0(|\mathbf{k}_1 + 2\mathbf{k}_2| r) \right]. \quad (12)$$

While the above expression appears to require a 6-D integration, in fact it only requires a 3-D integration. This owes to the fact that all terms can be expressed in terms of the magnitudes of  $\mathbf{k}_1$  and  $\mathbf{k}_2$  and the angle between these vectors. Note that in deriving the above result we have assumed that for the denominator of Eq. (5) one-loop corrections to the power spectra are of negligible importance. As we will show in Sec. 4, for the range of scales that we will consider, this assumption appears to be reasonably accurate.

Finally, regarding the cosmological sensitivity of the matter LCF, we see from Eq. (12) that at tree-level the LCF is built from integrals over products of the linear matter power spectrum on different scales. Thus the cosmological dependence derives entirely from specifying the dependence of the linear power on cosmology. This can best be achieved with Boltzmann codes like CAMB (Lewis et al. 2000).

## 2.3 The galaxy line correlation function

We next turn to the issue of predicting the galaxy LCF (hereafter GLCF). There are two sources of non-Gaussianity that can contribute here, one stems from the relation between the galaxy over density field  $\delta_g$  and that of the matter – otherwise known as galaxy bias. The second from the fact that galaxies are a point sampled process and with the usual assumption that they share the same limiting properties for rare occupancy of micro-cells as a Poisson sampling process.

Firstly, for the galaxy bias, if we assume that the density field in real space obeys the cosmological principle, in that it is statistically homogeneous and isotropic on sufficiently large scales, one can argue that in this regime the relation between  $\delta_g$  and  $\delta$  should become linear (Fry & Gaztanaga 1993; Smith et al. 2007). For this case the bias simply drops out of the equations for the GLCF, i.e.  $\epsilon_g(\mathbf{x}) = \epsilon(\mathbf{x})$  and the galaxy and dark matter LCFs fully coincide.

On smaller scales non-linear terms enter the bias relation (Fry & Gaztanaga 1993; Smith et al. 2007). Furthermore, if the relation does not depend on the present day local density but on the density of the initial patches, then non-local bias terms can contribute (Catelan et al. 2000; McDonald & Roy 2009; Chan et al. 2012; Baldauf et al. 2012). For that reason we employ the Eulerian non-linear, non-local bias model that was proposed by McDonald & Roy (2009). In their model non-locality is introduced via a term which is quadratic in the tidal tensor  $s_{ij}(\mathbf{x}) \equiv [\partial_i \partial_j \nabla^{-2} - \frac{1}{3} \delta_{ij}^K] \delta(\mathbf{x})$ , such that the galaxy over-

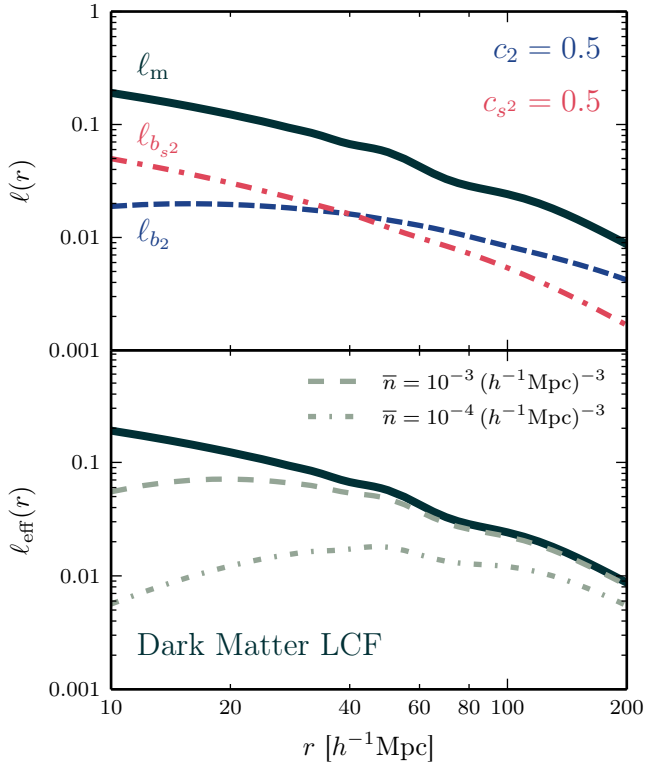


**Figure 1.** *Upper panel:* Comparison of various contributions to the galaxy LCF with  $\ell_{b_2}(r)$  in blue and  $\ell_{b_{s_2}}(r)$  in red. The coefficients  $c_2$  and  $c_{s_2}$  are both set to 0.5. *Lower panel:* Suppression effect from shot noise on the dark matter LCF, different line styles correspond to different number densities. The thick, black line in both panels is the LCF of the underlying matter field, i.e. for negligible shot noise.

density may be written as

$$\delta_g(\mathbf{x}) = b_1 \delta(\mathbf{x}) + \frac{1}{2} b_2 \left[ \delta^2(\mathbf{x}) - \langle \delta^2(\mathbf{x}) \rangle \right] + \frac{1}{2} b_{s_2} \left[ s^2(\mathbf{x}) - \langle s^2(\mathbf{x}) \rangle \right] + \dots, \quad (13)$$

where  $s^2 = s^{ij} s_{ji}$  and the dots indicate terms of even higher orders. The constants  $b_1$ ,  $b_2$ ,  $b_{s_2}$  denote the linear, non-linear and non-local bias terms, respectively, and the terms  $\langle \delta^2 \rangle$  as well as  $\langle s^2 \rangle$  ensure that  $\langle \delta_g \rangle = 0$ .

From the Fourier transform of Eq. (13) and by using PT we can readily determine the galaxy bispectrum. As before it can be expressed in terms of the linear dark matter power spectrum:

$$B_{g,123} = b_1^3 P_1 P_2 \left[ 2F_2(\mathbf{k}_1, \mathbf{k}_2) + c_2 + c_{s_2} S_2(\mathbf{k}_1, \mathbf{k}_2) \right] + \text{cyc.}, \quad (14)$$

where we used the short-hand notation  $B_{g,123} \equiv B_g(\mathbf{k}_1, \mathbf{k}_2, \mathbf{k}_3)$  and defined  $c_2 \equiv b_2/b_1$  and  $c_{s_2} \equiv b_{s_2}/b_1$ , and where we have neglected all higher order terms. We note that the non-local bias term has introduced an extra configuration dependence, which is encoded in the new kernel function (McDonald & Roy 2009):

$$S_2(\mathbf{k}_1, \mathbf{k}_2) = \left( \hat{\mathbf{k}}_1 \cdot \hat{\mathbf{k}}_2 \right)^2 - \frac{1}{3}. \quad (15)$$

Instead of relating the galaxy phase field to the matter one

via Eq. (13), we observe that the galaxy phase PDF can be obtained from the original PDF by replacing all spectra in its Edgeworth expansion with their biased equivalents. Hence, the three-point correlation of galaxy phase factors is the same as Eq. (5) with the dark matter quantities replaced by the galaxy bispectrum and power spectrum. As before we do not consider higher-order corrections to the denominator of Eq. (5), which are now also coming from non-linear and non-local bias, and simply substitute the linear galaxy power spectrum  $P_{L,g} = b_1^2 P_L$ . We thus find that the GLCF can be written to lowest order as the sum of three terms:

$$\ell_g(r) = \ell_m(r) + c_2 \ell_{b_2}(r) + c_{s_2} \ell_{b_{s_2}}(r), \quad (16)$$

where each term can be written:

$$\ell_\alpha(r) = \left( \frac{r}{4\pi} \right)^{9/2} \iint_{|\mathbf{k}_1|, |\mathbf{k}_2|, |\mathbf{k}_1 + \mathbf{k}_2| \leq 2\pi/r} d^3 \mathbf{k}_1 d^3 \mathbf{k}_2 \sqrt{\frac{P_1 P_2}{P_{12}}} \times \left[ j_0(|\mathbf{k}_2 - \mathbf{k}_1| r) + 2j_0(|\mathbf{k}_1 + 2\mathbf{k}_2| r) \right] \Gamma_\alpha(\mathbf{k}_1, \mathbf{k}_2), \quad (17)$$

where the above equation holds for  $\alpha \in \{m, b_2, b_{s_2}\}$  and where  $\Gamma_\alpha(\mathbf{k}_1, \mathbf{k}_2) = \{2F(\mathbf{k}_1, \mathbf{k}_2), 1, S_2(\mathbf{k}_1, \mathbf{k}_2)\}$ . At this point we draw attention to one of the major advantages of the GLCF over more conventional galaxy clustering statistics, which is that in the limit of linear bias, i.e. where  $b_2 = b_{s_2} = 0$ , we see that  $\ell_g(r) = \ell_m(r)$ . Hence it is a direct probe of the matter distribution, independent of linear bias. We also notice that in the presence of non-trivial biasing the GLCF is sensitive only to the relative bias parameters,  $c_2 = b_2/b_1$  and  $c_{s_2} = b_{s_2}/b_1$ .

Figure 1 (upper panel) shows all three terms. The dark matter LCF is indicated by the (black) thick line, and the dashed and dot-dashed lines represent the contribution of the local and nonlocal bias terms, respectively, where we set  $c_2 = c_{s_2} = 0.5$ . To evaluate the various expressions in Eq. (16) we adopted the same  $\Lambda$ CDM cosmology as described in Sec. 4 and generated the corresponding linear power spectrum using CAMB. We notice the different configuration dependence of all three functions, meaning that in principle it is possible to determine both  $c_2$  and  $c_{s_2}$ , as well as the amplitude of fluctuations  $\sigma_8$  from the LCF alone. However, the sole discernible difference between  $\ell_m(r)$  and  $\ell_{c_{s_2}}(r)$  are the damped BAO wiggles in the latter, so we cannot expect the LCF to yield strong constraints on  $c_{s_2}$ . We stress that for the bispectrum there will be a remaining degeneracy between  $\sigma_8$  and  $b_1$  as can be seen from Eq. (14), which must either be broken via a joint analysis with the power spectrum or under the inclusion of a cosmic microwave background (hereafter CMB) measurement.

For the remainder of this work we will additionally assume that bias is local in Lagrangian space, in which case it can be shown that the non-local bias term is related to the linear one at first order (Baldauf et al. 2012; Chan et al. 2012),

$$b_{s_2} = -\frac{4}{7} (b_1 - 1). \quad (18)$$

In this case galaxy biasing is only a function of two free parameters,  $b_1$  and  $b_2$ , and as we will show these can be efficiently constrained through combination of the LCF with the power spectrum.

## 2.4 The effect of shot noise on the GLCF

Another additional source of non-Gaussianity that modulates the GLCF is sampling noise. Any real measurement from a galaxy survey will be compromised by shot noise – the fact that the matter field has to be reconstructed from a discrete and finite set of tracers that have been sampled from some underlying field which may be Gaussian. This effect increases as the density of objects in a given volume decreases and leads to an artificial enhancement in the clustering strength of galaxies in the power spectrum. In the absence of a selection function and finite survey geometry, a constant number density of tracers  $\bar{n}$ , would modulate the true power spectrum and bispectrum as follows: (Peebles 1980; Matarrese et al. 1997),

$$P^{\text{d}}(k) = P(k) + \frac{1}{\bar{n}}, \quad (19)$$

$$B^{\text{d}}(k_1, k_2, k_3) = B_{123} + \frac{1}{\bar{n}} [P_1 + P_2 + P_3] + \frac{1}{\bar{n}^2}, \quad (20)$$

where the superscript d stands for the discrete case. All shot noise terms involving factors of  $1/\bar{n}$  can be subtracted to obtain an unbiased estimate of the true power spectrum or bispectrum, although they will still contribute to the errors.

To derive the effect of shot noise on the GLCF, we employ the same trick as employed in the last section. We assume the Fourier modes of the reconstructed matter field follow the same PDF as that of the true matter field, but with all spectra in the Edgeworth expansion replaced by the corresponding discrete quantities. Accordingly, using Eqs. (19) and (20) the three-point phase correlator estimated from a set of discrete tracers is given by

$$\begin{aligned} \langle \epsilon_{\mathbf{k}_1} \epsilon_{\mathbf{k}_2} \epsilon_{\mathbf{k}_3} \rangle^{\text{d}} &= \frac{(2\pi)^3}{V} \left( \frac{\sqrt{\pi}}{2} \right)^3 \sqrt{\frac{\nu_{\text{eff}}(k_1) \nu_{\text{eff}}(k_2) \nu_{\text{eff}}(k_3)}{V P_1 P_2 P_3}} \\ &\times \left[ B_{123} + \frac{1}{\bar{n}} (P_1 + P_2 + P_3) + \frac{1}{\bar{n}^2} \right] \\ &\times \delta_D(\mathbf{k}_1 + \mathbf{k}_2 + \mathbf{k}_3), \end{aligned} \quad (21)$$

where we have defined

$$\nu_{\text{eff}}(k) \equiv \frac{\bar{n} P(k)}{1 + \bar{n} P(k)}. \quad (22)$$

This factor encodes the shot noise contamination of each mode and is related to the effective volume of the survey (Tegmark 1997),

$$V_{\text{eff}}(k) = \int d^3x \left( \frac{\bar{n}(\mathbf{x}) P(k)}{1 + \bar{n}(\mathbf{x}) P(k)} \right)^2, \quad (23)$$

such that for a constant number density,  $\nu_{\text{eff}}(k) = \sqrt{V_{\text{eff}}(k)/V}$ .

The discrete form of the LCF can now be computed by substituting Eq. (21) into Eq. (3) and proceeding as before, whereupon we see that we may write the *effective* LCF as:

$$\hat{\ell}_{\text{eff}}(r) = \hat{\ell}^{\text{d}}(r) - \hat{\ell}_{\text{shot}}(r), \quad (24)$$

where the second term on the right-hand-side is a pure shot-

noise term which has the form:

$$\begin{aligned} \hat{\ell}_{\text{shot}}(r) &= 8\pi^2 \left( \frac{r}{4\pi} \right)^{9/2} \int_0^{2\pi/r} dk_1 k_1^2 \int_0^{2\pi/r} dk_2 k_2^2 \int_{-1}^{\mu_{\text{cut}}} d\mu \\ &\times \sqrt{\frac{\nu_{\text{eff}}(k_1) \nu_{\text{eff}}(k_2) \nu_{\text{eff}}(|\mathbf{k}_1 + \mathbf{k}_2|)}{\hat{P}_1 \hat{P}_2 \hat{P}_{12}}} \\ &\times \left[ \frac{1}{\bar{n}} (\hat{P}_1 + \hat{P}_2 + \hat{P}_{12}) + \frac{1}{\bar{n}^2} \right] j_0(|\mathbf{k}_2 - \mathbf{k}_1|r), \end{aligned} \quad (25)$$

where

$$\mu_{\text{cut}} = \min \left\{ 1, \max \left\{ -1, [(2\pi/r)^2 - k_1^2 - k_2^2] / 2k_1 k_2 \right\} \right\} \quad (26)$$

guarantees that  $|\mathbf{k}_1 + \mathbf{k}_2| \leq 2\pi/r$  and  $\hat{P}_{12} \equiv \hat{P}(|\mathbf{k}_1 + \mathbf{k}_2|)$ . Note that unlike  $P^{\text{d}}$  and  $B^{\text{d}}$  which may be fully corrected for ‘Poisson-like’ shot noise, the LCF can not (hence the name effective) since the shot noise contribution that enters via the factor  $\sqrt{\nu_{\text{eff}}(k_1) \dots / P_1^{\text{d}} \dots}$  in Eq. (21) can not be fully separated. Hence, it remains part of the estimator, but note that in the limit of  $\bar{n}P \gg 1$  the effect of shot-noise is negligible and we fully recover  $\ell_{\text{m}}$ . On the other hand, in the limit of  $\bar{n}P \ll 1$ , the estimate is shot noise dominated and the LCF scales as  $\propto 1/\sqrt{\bar{n}}$  multiplied by the three-point self-correlation function for a k-space top-hat filter function evaluated for a line configuration with the regularisation factor.

The subtraction of the shot-noise terms as described above leads to a suppression of the GLCF that has to be taken into account when comparing measurements to model predictions. Figure 1, bottom panel, shows the impact of this suppression effect on the true dark matter LCF (thick, solid line) for two different number densities. The smallest scales are most heavily affected, which is reasonable as most of the high  $k$ -modes are efficiently damped away by  $\nu_{\text{eff}}$ . Even for a number density of  $\bar{n} = 10^{-3} (h^{-1}\text{Mpc})^{-3}$  the suppression is significant, ranging from  $\sim 70\%$  at  $10 h^{-1}\text{Mpc}$  to still  $\sim 15\%$  at the scale of the first BAO bump ( $50 h^{-1}\text{Mpc}$ ). In Sec. 4 we will confront Eq. (21) with measurements from N-body simulations.

Before moving on, we note that the suppression of the GLCF due to point sampling can be understood in a rather intuitive way: when reconstructing the matter field, each tracer contributes with a single peak convolved with some narrow window function. If the density of tracers is decreased further and further, this field will tend to look like a collection of many separate peaks of nearly equal heights instead of reflecting the true underlying matter field with its density peaks of various heights and sizes. This leads to a suppression of phase correlations because the presence of many peaks with comparable heights renders the phase distribution nearly uniform, as has already been noted above (Hikage et al. 2004).

## 3 THE COVARIANCE OF THE LINE CORRELATION

In order to study how much cosmological information a combined measurement of the LCF and power spectrum provides, we will need to compute the auto-covariance properties of the LCF and its cross-covariance with the power

spectrum. The aim of this section is to provide analytic expressions for these quantities. Since this is a rather technical section, we suggest that for those not wishing to plough through the calculations at this stage they skip §3.2 and 3.3.

### 3.1 Estimators

In general we write the full joint covariance matrix of the LCF and power spectrum as:

$$C_{ij} \equiv \langle \delta X_i \delta X_j \rangle, \quad (27)$$

where  $\delta X_i = X_i - \langle X_i \rangle$  and  $X_i$  can either stand for the LCF estimator  $\hat{\ell}_i$  at some radial bin  $r_i$ , or the power spectrum estimator  $\hat{P}_i$  with bin  $k_i$ . In order to obtain expressions for the estimators of the theoretical definitions in Eqs. (3) and (6) we apply the following prescription: we assume that the survey volume is large enough to encompass many independent patches of the universe and hence replace the ensemble average with an average over volume. Performing the corresponding integrations, we are able to write the estimator for the LCF as:

$$\begin{aligned} \hat{\ell}(r) = & \frac{V^2}{(2\pi)^6} \left( \frac{r^3}{V} \right)^{3/2} \iint_{\substack{|\mathbf{k}_1|, |\mathbf{k}_2|, |\mathbf{k}_1 + \mathbf{k}_2| \leq 2\pi/r}} d^3 \mathbf{k}_1 d^3 \mathbf{k}_2 \\ & \times j_0(|\mathbf{k}_1 - \mathbf{k}_2| r) \epsilon_{\mathbf{k}_1} \epsilon_{\mathbf{k}_2} \epsilon_{-\mathbf{k}_1 - \mathbf{k}_2}. \end{aligned} \quad (28)$$

Similarly, for the power spectrum averaged over a bin of width  $\Delta k$ ,

$$\hat{P}(k) = \frac{1}{V} \int_k d^3 q_1 \int_k d^3 q_2 \frac{\delta_D(\mathbf{q}_1 + \mathbf{q}_2)}{V_P(k)} \delta_{q_1} \delta_{q_2}, \quad (29)$$

where the integrals run over  $|\mathbf{q}| \in [k - \Delta k/2, k + \Delta k/2]$  and  $V_P \equiv 4\pi k^2 \Delta k$  is the volume of a spherical shell in Fourier space.

Our main task is then to evaluate ensemble averages of phase factors  $\exp(i\theta_{\mathbf{k}})$  as well as combinations of phase factors with amplitudes  $A_{\mathbf{k}}$ , which are given as integrals over the joint PDF of Fourier modes  $\mathcal{P}(\{A_{\mathbf{k}}, \theta_{\mathbf{k}}\})$ . App. A demonstrates how this PDF can be expanded perturbatively in a series containing all higher order spectra, where the order of the contributing terms can be conveniently labeled by powers of  $1/\sqrt{V}$ . This expansion is then used to derive all ensemble averages to lowest order needed for the subsequent computations.

### 3.2 Auto-covariance matrix of $\hat{\ell}$

According to Eq. (27), the central quantity for the LCF covariance is the six-point phase correlator subtracted by the mean,

$$\mathcal{E}_{\ell\ell} \equiv \langle \epsilon_{\mathbf{k}_1} \epsilon_{\mathbf{k}_2} \epsilon_{\mathbf{k}_3} \epsilon_{\mathbf{q}_1} \epsilon_{\mathbf{q}_2} \epsilon_{\mathbf{q}_3} \rangle - \langle \epsilon_{\mathbf{k}_1} \epsilon_{\mathbf{k}_2} \epsilon_{\mathbf{k}_3} \rangle \langle \epsilon_{\mathbf{q}_1} \epsilon_{\mathbf{q}_2} \epsilon_{\mathbf{q}_3} \rangle, \quad (30)$$

where it is implied that  $\mathbf{k}_3 = -\mathbf{k}_1 - \mathbf{k}_2$  and  $\mathbf{q}_3 = -\mathbf{q}_1 - \mathbf{q}_2$ . Using the cumulant expansion theorem, we can split this correlator into its various connected pieces as follows,

$$\begin{aligned} \mathcal{E}_{\ell\ell} = & \langle \epsilon_{\mathbf{k}_1} \epsilon_{\mathbf{q}_1} \rangle \langle \epsilon_{\mathbf{k}_2} \epsilon_{\mathbf{q}_2} \rangle \langle \epsilon_{\mathbf{k}_3} \epsilon_{\mathbf{q}_3} \rangle + \text{sym.}(6) \\ & + \langle \epsilon_{\mathbf{q}_1} \epsilon_{\mathbf{k}_2} \epsilon_{\mathbf{k}_3} \rangle_c \langle \epsilon_{\mathbf{k}_1} \epsilon_{\mathbf{q}_2} \epsilon_{\mathbf{q}_3} \rangle_c + \text{sym.}(9) \\ & + \langle \epsilon_{\mathbf{k}_1} \epsilon_{\mathbf{k}_2} \epsilon_{\mathbf{q}_1} \epsilon_{\mathbf{q}_2} \rangle_c \langle \epsilon_{\mathbf{k}_3} \epsilon_{\mathbf{q}_3} \rangle + \text{sym.}(9) \\ & + \langle \epsilon_{\mathbf{k}_1} \epsilon_{\mathbf{k}_2} \epsilon_{\mathbf{k}_3} \epsilon_{\mathbf{q}_1} \epsilon_{\mathbf{q}_2} \epsilon_{\mathbf{q}_3} \rangle_c, \end{aligned} \quad (31)$$

with  $\text{sym.}(n)$  indicating that  $n - 1$  terms have to be added to symmetrize the corresponding expressions with respect to the  $\mathbf{k}$ 's and  $\mathbf{q}$ 's. Connected correlators consist of all those terms that cannot be written as a product of two or more connected pieces and for the phase fields they result from the PDF expansion coefficients where  $m = 1$  in Eq. (A6). As such, each connected phase correlator is not limited to a single spectrum but a series of all even or odd spectra, which become increasingly suppressed by factors of volume. The exception is the two-point function of phase factors, where statistical homogeneity dictates that  $\mathbf{k}_1 = -\mathbf{k}_2$ , in which case  $\epsilon_{\mathbf{k}_1} \epsilon_{\mathbf{k}_2} = |\epsilon_{\mathbf{k}_1}|^2$ , which is strictly one. Hence,

$$\langle \epsilon_{\mathbf{k}_1} \epsilon_{\mathbf{k}_2} \rangle = \frac{(2\pi)^3}{V} \delta_D(\mathbf{k}_1 + \mathbf{k}_2), \quad (32)$$

and we see that pairing either two  $\mathbf{k}$ - or  $\mathbf{q}$ -modes in  $\mathcal{E}_{\ell\ell}$  causes the respective third wavevector to be zero, meaning that it must belong to the background. These modes do not contribute to the correlation functions and consequently all those terms were left out in Eq. (31).

Since one of the three Dirac delta functions is redundant and  $\delta_D(\mathbf{0}) = V/(2\pi)^3$ , the Gaussian part of Eq. (31) is of fourth order, i.e. of order  $1/V^2$ . The second line is a product of two three-point correlators, which are given by Eq. (5) and by eliminating one of the two delta functions we have,

$$\begin{aligned} \langle \epsilon_{\mathbf{q}_1} \epsilon_{\mathbf{k}_2} \epsilon_{\mathbf{k}_3} \rangle_c \langle \epsilon_{\mathbf{k}_1} \epsilon_{\mathbf{q}_2} \epsilon_{\mathbf{q}_3} \rangle_c = & \frac{(2\pi)^3}{V} \left( \frac{\sqrt{\pi}}{2} \right)^6 \delta_D(\mathbf{k}_1 + \mathbf{q}_1) \\ & \times p^{(3)}(\mathbf{q}_1, \mathbf{k}_2, \mathbf{k}_3) p^{(3)}(\mathbf{k}_1, \mathbf{q}_2, \mathbf{q}_3). \end{aligned} \quad (33)$$

The quantities  $p^{(N)}$  refer to the reduced  $N$ -th order spectra, which are defined in Eq. (A4) and have a volume dependence of  $\propto V^{N/2-1}$ . This implies that the expression above is of the same order as the Gaussian term, such that higher order corrections to the three-point correlator do not have to be taken into account. The next two contributions to  $\mathcal{E}_{\ell\ell}$  contain connected four- and six-point correlators, which are worked out in App. A1 and A2, giving the following results to lowest order,

$$\begin{aligned} \langle \epsilon_{\mathbf{q}_1} \epsilon_{\mathbf{k}_2} \epsilon_{\mathbf{q}_1} \epsilon_{\mathbf{q}_2} \rangle_c \langle \epsilon_{\mathbf{k}_3} \epsilon_{\mathbf{q}_3} \rangle = & \frac{(2\pi)^3}{V} \left( \frac{\sqrt{\pi}}{2} \right)^4 \delta_D(\mathbf{k}_3 + \mathbf{q}_3) \\ & \times p^{(4)}(\mathbf{k}_1, \mathbf{k}_2, \mathbf{q}_1, \mathbf{q}_2), \end{aligned} \quad (34)$$

$$\langle \epsilon_{\mathbf{k}_1} \epsilon_{\mathbf{k}_2} \epsilon_{\mathbf{k}_3} \epsilon_{\mathbf{q}_1} \epsilon_{\mathbf{q}_2} \epsilon_{\mathbf{q}_3} \rangle_c = \left( \frac{\sqrt{\pi}}{2} \right)^6 p^{(6)}(\mathbf{k}_1, \mathbf{k}_2, \mathbf{k}_3, \mathbf{q}_1, \mathbf{q}_2, \mathbf{q}_3). \quad (35)$$

Having all necessary ingredients, we can plug the phase correlators back into Eq. (27) and perform the trivial Fourier integrations over the delta functions. Summing up all contributions in Eq. (31), it is possible to show that

$$\langle \delta \hat{\ell}_i \delta \hat{\ell}_j \rangle = \left[ \frac{(r_i r_j)^3}{V^2} \right]^{3/2} \left\{ \mathcal{C}_G + \mathcal{C}_T + \mathcal{C}_{B^2} + \mathcal{C}_{P_6} \right\}, \quad (36)$$

with

$$\begin{aligned} \mathcal{C}_G \equiv & \iint_{\substack{|\mathbf{k}_1|, |\mathbf{k}_2|, \\ |\mathbf{k}_1 + \mathbf{k}_2| \leq 2\pi/r}} \frac{d^3 \mathbf{k}_1}{k_f^3} \frac{d^3 \mathbf{k}_2}{k_f^3} \\ & \times \left[ j_0(|2\mathbf{k}_1 + \mathbf{k}_2| r_i) \mathcal{J}(\mathbf{k}_1, \mathbf{k}_2, r_j) + (r_i \leftrightarrow r_j) \right], \end{aligned} \quad (37)$$

$$\begin{aligned} \mathcal{C}_T &\equiv \left(\frac{\sqrt{\pi}}{2}\right)^4 \int_{|\mathbf{q}| \leq 2\pi/r} \frac{d^3 \mathbf{q}}{k_f^3} \int_{\substack{|\mathbf{k}_1|, |\mathbf{k}_1 + \mathbf{q}| \\ \leq 2\pi/r_i}} \frac{d^3 \mathbf{k}_1}{k_f^3} \int_{\substack{|\mathbf{k}_2|, |\mathbf{k}_2 + \mathbf{q}| \\ \leq 2\pi/r_j}} \frac{d^3 \mathbf{k}_2}{k_f^3} \\ &\times \mathcal{J}(\mathbf{q}, \mathbf{k}_1, r_i) \mathcal{J}(\mathbf{q}, \mathbf{k}_2, r_j) \\ &\times p^{(4)}(\mathbf{q}, \mathbf{k}_1, \mathbf{k}_2, -\mathbf{q} - \mathbf{k}_1 - \mathbf{k}_2), \end{aligned} \quad (38)$$

$$\begin{aligned} \mathcal{C}_{B^2} &\equiv \left(\frac{\sqrt{\pi}}{2}\right)^6 \int_{|\mathbf{q}| \leq 2\pi/r} \frac{d^3 \mathbf{q}}{k_f^3} \left[ \left( \int_{\substack{|\mathbf{k}_1|, |\mathbf{k}_1 + \mathbf{q}| \\ \leq 2\pi/r_i}} \frac{d^3 \mathbf{k}_1}{k_f^3} \mathcal{J}(\mathbf{q}, \mathbf{k}_1, r_i) \right. \right. \\ &\left. \left. \times p^{(3)}(\mathbf{q}, \mathbf{k}_1, -\mathbf{q} - \mathbf{k}_1) \right) \times \left( r_i \leftrightarrow r_j \right) \right], \end{aligned} \quad (39)$$

$$\begin{aligned} \mathcal{C}_{P_6} &\equiv \left(\frac{\sqrt{\pi}}{2}\right)^6 \iint_{\substack{|\mathbf{k}_1|, |\mathbf{k}_2|, \\ |\mathbf{k}_1 + \mathbf{k}_2| \leq 2\pi/r_i}} \frac{d^3 \mathbf{k}_1}{k_f^3} \frac{d^3 \mathbf{k}_2}{k_f^3} \iint_{\substack{|\mathbf{q}_1|, |\mathbf{q}_2|, \\ |\mathbf{q}_1 + \mathbf{q}_2| \leq 2\pi/r_j}} \frac{d^3 \mathbf{q}_1}{k_f^3} \frac{d^3 \mathbf{q}_2}{k_f^3} \\ &\times j_0(|\mathbf{k}_1 - \mathbf{k}_2| r_i) j_0(|\mathbf{q}_1 - \mathbf{q}_2| r_j) \\ &\times p^{(6)}(\mathbf{k}_1, \mathbf{k}_2, \mathbf{k}_3, \mathbf{q}_1, \mathbf{q}_2, \mathbf{q}_3), \end{aligned} \quad (40)$$

where we have defined the kernel function

$$\mathcal{J}(\mathbf{k}_1, \mathbf{k}_2, r) \equiv 2j_0(|\mathbf{k}_1 - \mathbf{k}_2| r) + j_0(|2\mathbf{k}_1 + \mathbf{k}_2| r). \quad (41)$$

Furthermore,  $k_f \equiv 2\pi/V^{1/3}$  denotes the fundamental frequency and  $r \equiv \max\{r_i, r_j\}$ . We note that Eq. (36) closely resembles the covariance of the bispectrum (see [Sefusatti et al. 2006](#)) with a Gaussian term, one that is quadratic in the bispectrum as well as terms proportional to the trispectrum and the sixth-order spectrum. However, one important difference is that there is no cosmology dependence in the Gaussian contribution, which is a direct consequence of the two-point phase correlator in Eq. (32), that carries no information either. That means that Eq. (37) is just an algebraic expression depending on the scales  $r_i$  and  $r_j$ , and for the variance we get explicitly,

$$\text{Var}(\hat{\ell}(r)) \approx 0.25 \frac{r^3}{V}. \quad (42)$$

### 3.3 Cross-covariance matrix between $\hat{P}$ and $\hat{\ell}$

Analogously to the last section we can now derive the cross-covariance between LCF and power spectrum. In this case we deal with a mixed five-point correlator of phase factors and amplitudes,

$$\mathcal{E}_{P\ell} \equiv \langle \delta_{\mathbf{k}_1} \delta_{\mathbf{k}_2} \epsilon_{\mathbf{q}_1} \epsilon_{\mathbf{q}_2} \epsilon_{\mathbf{q}_3} \rangle - \langle \delta_{\mathbf{k}_1} \delta_{\mathbf{k}_2} \rangle \langle \epsilon_{\mathbf{q}_1} \epsilon_{\mathbf{q}_2} \epsilon_{\mathbf{q}_3} \rangle. \quad (43)$$

Let us again begin by splitting this expression into its connected correlators, giving

$$\begin{aligned} \mathcal{E}_{P\ell} &= [\langle \delta_{\mathbf{k}_1} \epsilon_{\mathbf{q}_1} \rangle \langle \delta_{\mathbf{k}_2} \epsilon_{\mathbf{q}_2} \epsilon_{\mathbf{q}_3} \rangle_c + \text{sym.}(3)] + (\mathbf{k}_1 \leftrightarrow \mathbf{k}_2) \\ &+ \langle \delta_{\mathbf{k}_1} \delta_{\mathbf{k}_2} \epsilon_{\mathbf{q}_1} \epsilon_{\mathbf{q}_2} \epsilon_{\mathbf{q}_3} \rangle_c, \end{aligned} \quad (44)$$

where we have left out all terms that give rise to background modes as before. Due to statistical homogeneity the mixed two-point correlator is simply the average of the amplitude  $|\delta_{\mathbf{k}}|$ , which must be evaluated using the joint PDF of Fourier modes described in App. A. Assuming temporarily that we are having a discrete set of modes, the Gaussian part is given

by (see Eqs. A2 and A9)

$$\begin{aligned} \langle \delta_{\mathbf{k}} \epsilon_{\mathbf{q}} \rangle &= \sqrt{V P(k)} \int \prod_{\mathbf{p} \in \text{uhs}} 2A_{\mathbf{p}} e^{-A_{\mathbf{p}}^2} dA_{\mathbf{p}} \frac{d\theta_{\mathbf{p}}}{2\pi} A_{\mathbf{k}} e^{i(\theta_{\mathbf{k}} + \theta_{\mathbf{q}})} \\ &= \frac{\sqrt{\pi}}{2} \sqrt{V P(k)} \int \prod_{\mathbf{p} \in \text{uhs}} \frac{d\theta_{\mathbf{p}}}{2\pi} e^{i(\theta_{\mathbf{k}} + \theta_{\mathbf{q}})} \\ &= \frac{\sqrt{\pi}}{2} \sqrt{V P(k)} \delta_{\mathbf{k} + \mathbf{q}}, \end{aligned} \quad (45)$$

where the products run over all modes  $\mathbf{p}$  in the upper half sphere (uhs), defined by  $p_z \geq 0$ . In going from the first to the second line we have made use of Eq. (A13) to do the integrals over  $A_{\mathbf{p}}$  and then we see that the remaining integrals only give a non-vanishing result if the two phases cancel out each other. The square root factor of the power spectrum enters because of our choice of normalization, i.e.  $|\delta_{\mathbf{k}}| \equiv \sqrt{V P(k)} A_{\mathbf{k}}$ . Finally, taking the continuum limit,

$$\langle \delta_{\mathbf{k}} \epsilon_{\mathbf{q}} \rangle = \frac{(2\pi)^3}{V} \frac{\sqrt{\pi}}{2} \sqrt{V P(k)} \delta_D(\mathbf{k} + \mathbf{q}). \quad (46)$$

In a similar manner we can compute the mixed three-point correlator and we consider the case where  $\mathbf{q}_1, \mathbf{q}_2 \in \text{uhs}$ , while  $\mathbf{k} \in \text{lhs}$ . The lowest order term that is contributing is proportional to the reduced bispectrum and we have,

$$\begin{aligned} \langle \delta_{\mathbf{k}} \epsilon_{\mathbf{q}_1} \epsilon_{\mathbf{q}_2} \rangle_c &= \sqrt{V P(k)} \int \prod_{\mathbf{p} \in \text{uhs}} 2A_{\mathbf{p}} e^{-A_{\mathbf{p}}^2} dA_{\mathbf{p}} \frac{d\theta_{\mathbf{p}}}{2\pi} \\ &\times \sum_{\substack{\mathbf{u}_1, \mathbf{u}_2, \mathbf{u}_3 \in \text{uhs} \\ \mathbf{u}_i \neq \mathbf{u}_j}} A_{\mathbf{u}_1} A_{\mathbf{u}_2} A_{\mathbf{u}_3} \cos(\theta_{\mathbf{u}_1} + \theta_{\mathbf{u}_2} - \theta_{\mathbf{u}_3}) \\ &\times p^{(3)}(\mathbf{u}_1, \mathbf{u}_2, \mathbf{u}_3) A_{\mathbf{k}} e^{i(\theta_{\mathbf{q}_1} + \theta_{\mathbf{q}_2} - \theta_{\mathbf{k}})}. \end{aligned} \quad (47)$$

The phase factors can only be fully cancelled in the case where  $\mathbf{k}$  equals  $\mathbf{u}_3$ , such that the integrals over  $A_{\mathbf{p}}$  produce a factor of  $(\sqrt{\pi}/2)^2$ . For the remaining phase integrals we need to impose the condition  $\mathbf{k} + \mathbf{q}_1 + \mathbf{q}_2 = 0$  and hence, the final result after taking the continuum limit is

$$\begin{aligned} \langle \delta_{\mathbf{k}} \epsilon_{\mathbf{q}_1} \epsilon_{\mathbf{q}_2} \rangle_c &= \frac{(2\pi)^3}{V} \left(\frac{\sqrt{\pi}}{2}\right)^2 \sqrt{V P(k)} p^{(3)}(\mathbf{k}, \mathbf{q}_1, \mathbf{q}_2) \\ &\times \delta_D(\mathbf{k} + \mathbf{q}_1 + \mathbf{q}_2). \end{aligned} \quad (48)$$

One can check that this result holds for any configuration of the three vectors  $\mathbf{k}, \mathbf{q}_1$  and  $\mathbf{q}_2$ . The calculation of the connected five-point correlator is more cumbersome and is therefore carried out in App. A3, giving the simple outcome

$$\begin{aligned} \langle \delta_{\mathbf{k}_1} \delta_{\mathbf{k}_2} \epsilon_{\mathbf{q}_1} \epsilon_{\mathbf{q}_2} \epsilon_{\mathbf{q}_3} \rangle_c &= (2\pi)^3 \left(\frac{\sqrt{\pi}}{2}\right)^3 \sqrt{P(k_1) P(k_2)} \\ &\times p^{(5)}(\mathbf{k}_1, \mathbf{k}_2, \mathbf{q}_1, \mathbf{q}_2, \mathbf{q}_3) \\ &\times \delta_D(\mathbf{k}_1 + \mathbf{k}_2 + \mathbf{q}_1 + \mathbf{q}_2 + \mathbf{q}_3). \end{aligned} \quad (49)$$

Finally, assembling all these pieces in Eq. (44) and plugging back into Eq. (27) we obtain,

$$\langle \delta \hat{\ell}_i \delta \hat{P}_j \rangle = \frac{1}{k_f^3} \left(\frac{\sqrt{\pi}}{2}\right)^3 \left(\frac{r_i^3}{V}\right)^{3/2} \left[ \mathcal{C}_{PB} + \mathcal{C}_{P_5} \right], \quad (50)$$

with

$$\mathcal{C}_{PB} \equiv 2\Theta_{ij} P(k_j) \int_{|\mathbf{q}|, |\mathbf{q}+\mathbf{k}_j| \leq 2\pi/r_i} d^3q j_0(|\mathbf{k}_j - \mathbf{q}|r_i) \times p^{(3)}(\mathbf{k}_j, \mathbf{q}, -\mathbf{k}_j - \mathbf{q}), \quad (51)$$

and

$$\mathcal{C}_{P_5} \equiv \frac{1}{V_P(k_j)} \int_{k_j} d^3p \iint_{\substack{|\mathbf{q}_1|, |\mathbf{q}_2|, \\ |\mathbf{q}_1+\mathbf{q}_2| \leq 2\pi/r_i}} d^3q_1 d^3q_2 j_0(|\mathbf{q}_1 - \mathbf{q}_2|r_i) \times P(p) p^{(5)}(\mathbf{p}, -\mathbf{p}, \mathbf{q}_1, \mathbf{q}_2, \mathbf{q}_3). \quad (52)$$

Here,  $\Theta_{ij}$  stands for the theta function  $\Theta(1 - k_j r_i/2\pi)$ , indicating that we only get a correlation at the order of the bispectrum if the power spectrum scale  $k_j$  lies outside of the region affected by the LCF cutoff. As for the LCF auto-covariance we notice a strong similarity to the bispectrum and power spectrum cross-covariance given in [Sefusatti et al. \(2006\)](#).

### 3.4 Signal-to-noise

In summary, we see that the LCF covariance closely resembles the covariance of the bispectrum. Its leading order term is much simpler, though, as it carries no cosmological information – this enters only through higher order terms. In the large-scale limit the LCF covariance is therefore independent of redshift and shot noise. On the other hand the lowest order contribution to the cross-covariance between  $\hat{P}$  and  $\hat{\ell}$  contains cosmological information from both, the power spectrum and the bispectrum.

Based on the results from the previous section, it is instructive to compare the cumulative signal-to-noise of the LCF with that of the power spectrum in the Gaussian approximation. To plot both as a function of the maximal mode  $k_{\max}$  included, we use the correspondence  $r = \pi/k$ , so that we can write the LCF signal-to-noise as follows

$$\left(\frac{\mathcal{S}}{\mathcal{N}}\right)_{\ell}^2 = \sum_{i=1}^{i_{\max}} \sum_{j=1}^{i_{\max}} \ell_{\text{eff}}(r_i) C_{ij}^{-1} \ell_{\text{eff}}(r_j), \quad (53)$$

where  $r_i = \pi/(i \delta k)$  and  $i_{\max} = k_{\max}/\delta k$ . The signal  $\ell_{\text{eff}}(r)$  denotes the discrete LCF subtracted by the shot noise terms that appear in the square bracket of Eq. (21) and hence takes the suppression due to  $\nu_{\text{eff}}$  into account (explicit expressions are given in Eqs. 24 and 25).

The Gaussian part of the covariance matrix for the power spectrum estimator in Eq. (29) is diagonal and given by ([Feldman et al. 1994](#))

$$\sigma_P^2(k) = \frac{2(2\pi)^3}{V_P(k)V} \left( P(k) + \frac{1}{\bar{n}} \right)^2 = \frac{2(2\pi)^3}{V_P(k)} \frac{P(k)}{V_{\text{eff}}(k)}, \quad (54)$$

with  $P(k)$  meaning the discrete power spectrum subtracted by its shot noise component and  $V_{\text{eff}}$  the effective volume introduced in Eq. (23). Writing  $k = i \delta k$  the signal-to-noise is thus

$$\left(\frac{\mathcal{S}}{\mathcal{N}}\right)_P^2 = \sum_{i=1}^{i_{\max}} \frac{P(k)^2}{\sigma_P^2(k)} = \sum_{i=1}^{i_{\max}} \frac{V_P(k)}{2(2\pi)^3} V_{\text{eff}}(k). \quad (55)$$

In Fig. 2 we plot Eqs. (53) and (55) for various number densities as a function of  $k_{\max}$  ( $r_{\min}$ ), where we assumed a cubical

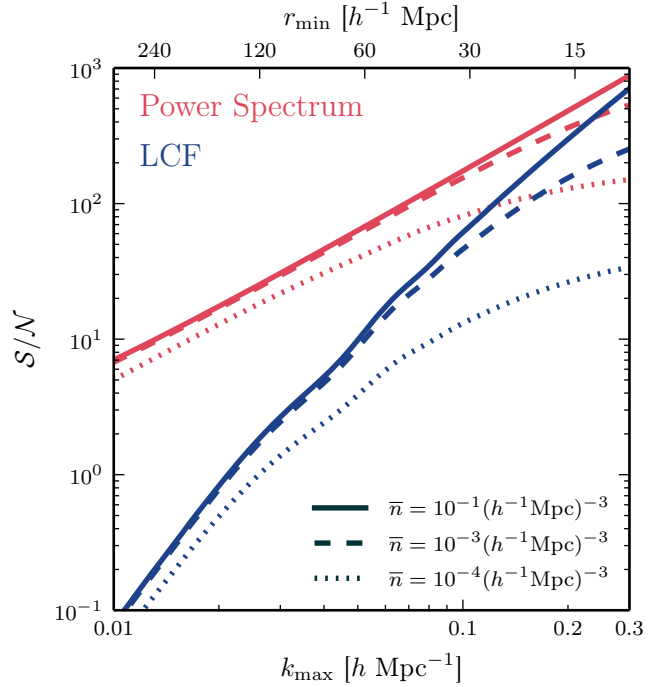


**Figure 2.** Cumulative signal-to-noise for the power spectrum (red) and LCF (blue) based on Eqs. (55) and (53) as a function of the maximal mode  $k_{\max}$  or minimal scale  $r_{\min}$ , which are related via  $r_{\min} = \pi/k_{\max}$ . We consider three different galaxy number densities:  $\bar{n} = 10^{-3} (h^{-1} \text{Mpc})^{-3}$  (solid lines),  $10^{-4} (h^{-1} \text{Mpc})^{-3}$  (dashed) and  $10^{-5} (h^{-1} \text{Mpc})^{-3}$  (dotted).

survey volume with sidelength  $L = 1.5 h^{-1} \text{Gpc}$  and used a bin width of  $\delta k = 2\pi/L$ . As before, we adopted a  $\Lambda\text{CDM}$  cosmology with parameters described in Sec. 4 and computed the LCF in linear PT. We see that, for most of the scales that we have considered,  $k_{\max} < 0.3 h \text{Mpc}^{-1}$ , the power spectrum signal-to-noise dominates over that of the LCF, being comparable only for  $k_{\max} \sim 0.3 h \text{Mpc}^{-1}$  and the densest galaxy sample. However, the LCF signal-to-noise increases more quickly as a function of  $k_{\max}$ , which is a recognized feature of higher-order statistics ([Sefusatti & Scoccimarro 2005](#)). On the other hand, the LCF is also more heavily impacted by shot noise than the power spectrum. While the difference in signal-to-noise at  $k_{\max} = 0.3 h \text{Mpc}^{-1}$  is  $\sim 10\%$  for the highest number density it is already  $\sim 75\%$  for the lowest. This is because each mode contributing to the signal-to-noise is penalized by a factor of  $\nu_{\text{eff}}$ , so for an  $N$ -th order statistic we should expect a suppression proportional to  $\nu_{\text{eff}}^N$ .

Finally, we note that here we are only probing a subset of the available information in the three-point phase correlation as the definition of the LCF in Eq. (3) forces the three points of the triangle to lie along a line – so called degenerate triangles. Adding measurements with various other triangle configurations is certainly going to increase the signal-to-noise. Another possibility to boost the signal-to-noise is to find a more optimal mode cutoff than the top-hat window used in the definition of the LCF, which could for instance be done in the Gaussian approximation of Eq. (36).



## 4 COMPARISON WITH $N$ -BODY SIMULATIONS

### 4.1 Numerical simulations

In this section we present measurements of the LCF and its covariance matrix along with the cross-correlation of the LCF with the power spectrum. These measurements are based on a set of 200 dark matter only  $N$ -body simulations, which were run on the ZBOX2 and ZBOX3 supercomputers at the University of Zurich (see Sec. 6 of Smith 2009) using the Gadget-2 code of Springel (2005). The simulations contain  $750^3$  particles, which are enclosed in a periodic box of co-moving size  $L = 1500 h^{-1}$  Mpc. Initial conditions were set up at redshift  $z = 49$  based on different realizations of a Gaussian random field and second order Lagrangian perturbation theory (Crocco & Scoccimarro 2006) for the displacement of the particles. The power spectrum of the Gaussian random fields was determined from a transfer function generated by CMBFAST (Seljak & Zaldarriaga 1996) assuming a flat  $\Lambda$ CDM model with cosmological parameters  $\Omega_m = 0.25$ ,  $\Omega_b = 0.04$ ,  $\sigma_8 = 0.8$ ,  $n_s = 1.0$  and  $h = 0.7$ .

### 4.2 Estimating $\hat{P}$ in simulations

From the simulations we construct smooth dark matter density fields by distributing the particles onto a grid using a cloud-in-cell (CIC) assignment scheme with  $N = 512$  cells per side. Each Fourier mode of the resulting field is then corrected for the convolution with the mesh by dividing out the Fourier transform of the CIC window function:

$$\delta_{\mathbf{k}}^d = \frac{\delta_{\mathbf{k}}^g}{W_{\text{CIC}}(\mathbf{k})}, \quad (56)$$

where

$$W_{\text{CIC}}(\mathbf{k}) = \prod_{i=1}^3 \left[ \frac{\sin(\pi k_i / 2k_{\text{Ny}})}{\pi k_i / 2k_{\text{Ny}}} \right]^2. \quad (57)$$

The superscripts  $d$  and  $g$  denote discrete and grid quantities, respectively, and  $k_{\text{Ny}} = \pi N_{\text{grid}}/L$  is the Nyquist frequency of the mesh, with  $N_{\text{grid}}$  being the number of mesh-cells per dimension.

For the power spectrum estimator presented in Eq. (29) it can be shown that for a finite periodic volume it can be rewritten for a given scale  $k$  as:

$$\hat{P}^d(k) = \frac{V}{N_k} \sum_{|k-q_i| \leq \Delta k/2} \left| \delta_{\mathbf{q}_i}^d \right|^2, \quad (58)$$

where the sum extends over all modes within a shell of thickness  $\Delta k$  centered around  $k$ , and where  $N_k$  is the number of Fourier modes in each shell. This estimate still suffers from discreteness effects, and at late times when the initial transients are small, an unbiased estimate is therefore obtained by subtracting the shot noise term, i.e.  $\hat{P} = \hat{P}^d - 1/\bar{n}$ , where  $\bar{n} = N/V$ , with  $N$  being the number of dark matter particles. In the following we consider measurements of the power spectrum in 30 bins from  $k_{\text{min}} = 0.005$  till  $k_{\text{max}} = 0.3 h \text{ Mpc}^{-1}$  and a bin width of  $\Delta k = 0.01 h \text{ Mpc}^{-1}$ . The power spectrum is also susceptible to aliasing effects, hence we also use FFT grids for which  $k_{\text{Ny}} > 2k_{\text{max}}$ .

### 4.3 Estimating $\hat{\ell}$ in simulations

The discretized version of the LCF estimator given by Eq. (28) can be written in the form:

$$\text{E1: } \hat{\ell}^d(r) = \left( \frac{r^3}{V} \right)^{3/2} \sum_{\substack{|\mathbf{k}_1|, |\mathbf{k}_2|, \\ |\mathbf{k}_1 + \mathbf{k}_2| \leq 2\pi/r}} \bar{j}_0(|\mathbf{k}_1 - \mathbf{k}_2|r) \epsilon_{\mathbf{k}_1}^d \epsilon_{\mathbf{k}_2}^d \epsilon_{-\mathbf{k}_1 - \mathbf{k}_2}^d, \quad (59)$$

where  $\bar{j}_0(|\mathbf{k}|r)$  denotes the spherical Bessel function averaged over the  $k$ -space volume centred on the Fourier mode  $\mathbf{k}$ . We found that this estimator is computationally expensive to estimate, at least for the case where  $r$  is probing small scales, since the 6D sum in Eq. (59) runs over the majority of Fourier modes – the worst case being  $\mathcal{O}(N_{\text{grid}}^6)$  terms.

In order to accelerate the estimation we employ an implementation based on the real space phase fields. The estimator is built around Eq. (1): we take the product of the  $\epsilon_r(\mathbf{x})$  values at three different points separated by scale  $r$  and average these over all possible positions and orientations of the three points in a line (see also the appendix of Eggeheimer et al. 2015). The new estimator can be written:

$$\text{E2: } \hat{\ell}^d(r) = \left( \frac{r^3}{V} \right)^{3/2} \frac{\Delta\varphi \Delta\vartheta}{16\pi} \sum_{\mathbf{x}} \sum_{i,j=0}^n w_i w_j \sin(j \Delta\vartheta) \\ \times \epsilon_r^d(\mathbf{x}) \epsilon_r^d(\mathbf{x} + \mathbf{r}_{ij}) \epsilon_r^d(\mathbf{x} - \mathbf{r}_{ij}), \quad (60)$$

where the sum over  $\mathbf{x}$  averages over all points in the volume, and the sums over  $i$  and  $j$  discretize the angular integration of the orientation of the line  $\hat{\mathbf{r}}$  over all orientations, with  $i$  labeling the azimuthal angle and  $j$  the angle with respect to the polar axis. The angular bin sizes are  $\Delta\varphi = 2\pi/n$  and  $\Delta\vartheta = \pi/n$ . The weight factors come from the trapezoidal rule for numerical integration and are either  $w_i = 1$  if  $i = 0$  or  $n$  and 2 otherwise. The radial vector is defined by  $\mathbf{r}_{ij} \equiv r \mathbf{e}_r(i, j)$ , where the unit vector is specified by

$$\mathbf{e}_r(i, j) \equiv \begin{pmatrix} \sin \vartheta \cos \varphi \\ \sin \vartheta \sin \varphi \\ \cos \vartheta \end{pmatrix} = \begin{pmatrix} \sin(j \Delta\vartheta) \cos(i \Delta\varphi) \\ \sin(j \Delta\vartheta) \sin(i \Delta\varphi) \\ \cos(j \Delta\vartheta) \end{pmatrix}. \quad (61)$$

Note that owing to the fact that the phase field is smoothed on scale  $r$  (see Eq. 2),  $\epsilon_r^d(\mathbf{x})$  has to be recomputed for each new scale for which  $\ell$  is estimated. This however can be rapidly performed by applying the cutoff in Fourier space and executing an inverse Fast Fourier Transform, i.e.

$$\epsilon_r^d(\mathbf{x}) = \text{iFFT} \left[ \epsilon_{\mathbf{k}}^d \Theta \left( 1 - \frac{k r}{2\pi} \right) \right]. \quad (62)$$

Lastly, for the case of estimation in the  $N$ -body simulations, any point that gets mapped outside of the box is placed back according to the periodic boundary conditions.

From a number of tests we have found that the numerical estimator above converges already for a moderate number of bins, which is of the order 10. That means E2 requires of the order  $100 N^3$  operations, independent of the scale  $r$ , while E1 scales as  $\sim (2L/r)^6$  after the mode cutoff as taken into account. This implies that E2 quickly becomes more efficient at scales  $r \lesssim 10^{-1/3} \times 2L/\sqrt{N}$ , i.e.  $r \lesssim 60 h^{-1} \text{ Mpc}$  for  $N = 512$ .

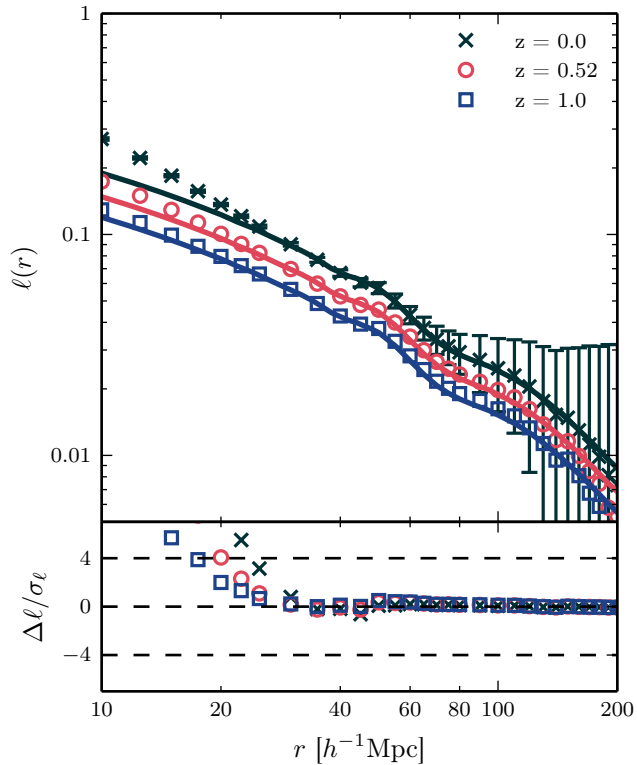


**Figure 3.** The top panel displays the results of the LCF measurements from 200 N-body simulations (data points) for the three redshifts  $z = 0, 0.52$  and  $1$ , while the  $1\text{-}\sigma$  error bars for just shown for the lowest redshift sample. Solid lines of matching color are the corresponding predictions from tree-level perturbation theory. The bottom panel shows the relative difference between measured and predicted LCF, normalized by the  $1\text{-}\sigma$  standard deviation.

#### 4.4 Comparison of estimators with simulations

Figure 3, upper panel, shows the results for the matter LCF measured for three different redshifts  $z = 0, 0.52$  and  $1$ . The measurements were made for 30 bins with the line scale varying  $r \in [10, 200] h^{-1}\text{Mpc}$ , which on using the relation  $k \sim \pi/r$  roughly corresponds to a wavemode range of  $k \in [0.016, 0.31] h \text{Mpc}^{-1}$  and is hence comparable to our power spectrum measurements. The spacing of the first 7 bins is  $2.5 h^{-1}\text{Mpc}$ , increasing to  $5 h^{-1}\text{Mpc}$  for the next 11 and the remaining 12 bins have a spacing of  $10 h^{-1}\text{Mpc}$ . The error bars show the expected variations between realisations and are obtained from the 200 realisations. For the sake of clarity we only show the  $1\text{-}\sigma$  error bars for the sample with the lowest redshift. The estimates were corrected for shot noise as discussed in §2.4.

From the figure we see immediately how the LCF increases with time, which is a result of growing phase correlations under the influence of non-linear gravity. For the same reason the LCF is a function that is mostly decreasing with scale, as at larger  $r$  the density field is in a more linear state with phases being increasingly random. The solid lines in Fig. 3 show the predictions from tree-level SPT (see Eq. 12), and on large scales ( $r > 30 h^{-1}\text{Mpc}$ ) are in good agreement with the data for the three redshifts considered. However, on smaller scales we see that there are departures

from this lowest order prediction, which consistently underpredicts the measured LCF.

Figure 3, lower panel, shows the difference  $\Delta\ell = \hat{\ell} - \ell$  between the measurement and model predictions, normalized by the standard deviation. For all scales above  $\sim 30 h^{-1}\text{Mpc}$  the difference is within the  $1\text{-}\sigma$  interval, while for smaller scales the agreement breaks down quickly, being already worse than  $4\sigma$  at  $r = 20 h^{-1}\text{Mpc}$  and the lowest redshift. These deviations arise because non-linear corrections to the bispectrum and power spectrum become increasingly important on these small scales. This also explains why the discrepancies are less significant for higher redshifts. Changing the power spectrum model that enters Eq. (12) from the linear spectrum to the power spectrum with corrections up to the one-loop level does not bring any improvement. On the contrary, we note that the increase in small-scale power leads to a further suppression of the LCF and alters the predictions by  $1.4\sigma_\ell$  at  $r = 40 h^{-1}\text{Mpc}$ . This suppression will be countered when using the appropriate one-loop bispectrum, but this seems to indicate that linear theory is applicable throughout a larger range of scales for the LCF than it is for the conventional statistical measures.

#### 4.5 Testing the effects of shot-noise on $\hat{\ell}$

In the measurements above where all the dark matter particles have been used to construct the density field, shot noise has no discernible effect. To test the suppression from discreteness derived in Sec. 2.4 we therefore carry out the same measurements, but coming from a subsample of particles that is randomly selected before the particles are smoothed onto the grid. This procedure does not correspond to a Poisson sampling of the underlying matter field, but it should serve as a close enough approximation thereof. In the upper panel of Fig. 4 diamonds (squares) show the measured LCF for 1% (0.1%) of the total number of particles, compared to the original measurements (stars), whereas the solid lines of matching color are the theoretical predictions in tree-level SPT based on the bispectrum term in Eq. (21). We clearly see how the measurements get increasingly suppressed with decreasing number density and accurately follow the predictions, confirming our model.

#### 4.6 Testing the signal-to-noise of $\hat{\ell}$

The lower panel of Fig. 4 contrasts the measured cumulative signal-to-noise with the idealized case of Gaussian errors presented in Sec. 3.2, where the symbols are the same as in the upper panel and colors distinguish between power spectrum and LCF. For both number densities we notice that the measured signal-to-noise traces the predicted one very well up to a  $k_{\text{max}}$  of  $\sim 0.1 h \text{Mpc}^{-1}$ . Beyond this scale the measured signal-to-noise quickly flattens out because higher-order corrections to the power spectrum and LCF covariance diminish the amount of available information. As can be seen in the plot, this effect can be quite severe: at the largest  $k_{\text{max}}$  the power spectrum signal-to-noise is approximately reduced by a factor of three, while the LCF signal-to-noise even suffers by a factor of seven.

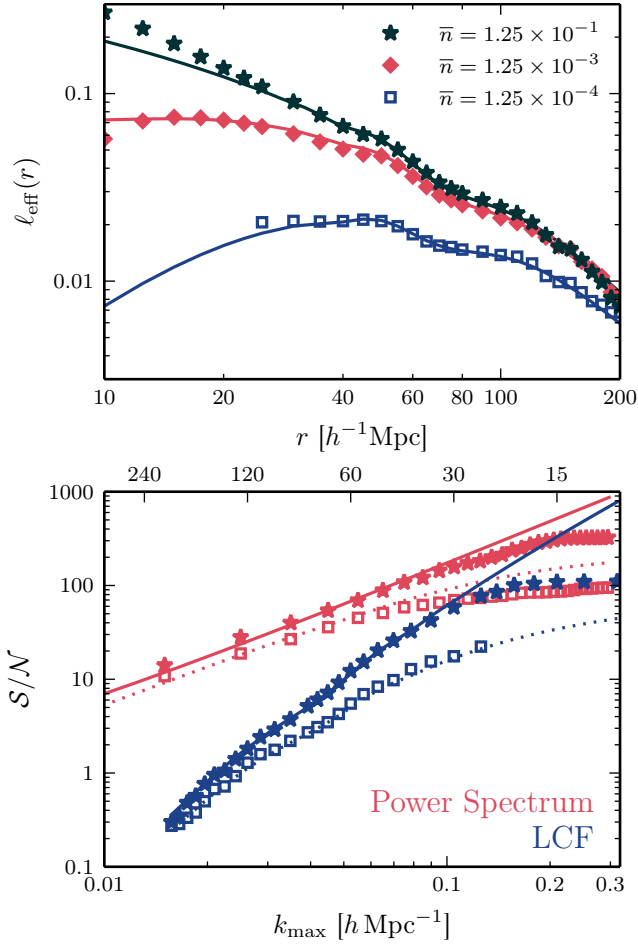


**Figure 4.** *Upper panel:* Estimated LCF at redshift  $z = 0.0$  for different particle densities (in units of  $h^{-3}\text{Mpc}^3$ ), corrected for additive shot noise terms. Stars mark the original measurements using all particles, diamonds (squares) derive from a subsample with 1% (0.1%) of the particles. Solid lines in the same color correspond to the tree-level predictions. *Lower panel:* Measured cumulative signal-to-noise for power spectrum (red) and LCF (blue), compared to the approximation with Gaussian errors (solid and dotted lines). Symbols are the same as in the upper panel.

#### 4.7 Estimating the covariance matrix

Apart from the means, it is also instructive to consider the covariance matrix of the power spectrum and LCF estimators. To begin with, in Fig. 5 we compare the measured LCF variance in all 30 bins with the Gaussian approximation (dashed line) from Eq. (42) for the same three redshifts as in Fig. 3. The error bars were estimated via Jackknife resampling, meaning we first computed the variance  $\sigma_\ell^2$  from the full sample of  $N_{\text{real}} = 200$  realizations and subsequently from  $N_{\text{real}}$  different subsamples, each giving  $(\sigma_\ell^{(i)})^2$ , in which the  $i$ -th realization has been left out. The error on the variance is then computed as follows (Norberg et al. 2009):

$$\delta\sigma_\ell^2 = \sqrt{\frac{N_{\text{real}} - 1}{N_{\text{real}}} \sum_{i=1}^{N_{\text{real}}} \left[ (\sigma_\ell^{(i)})^2 - \sigma_\ell^2 \right]^2}. \quad (63)$$

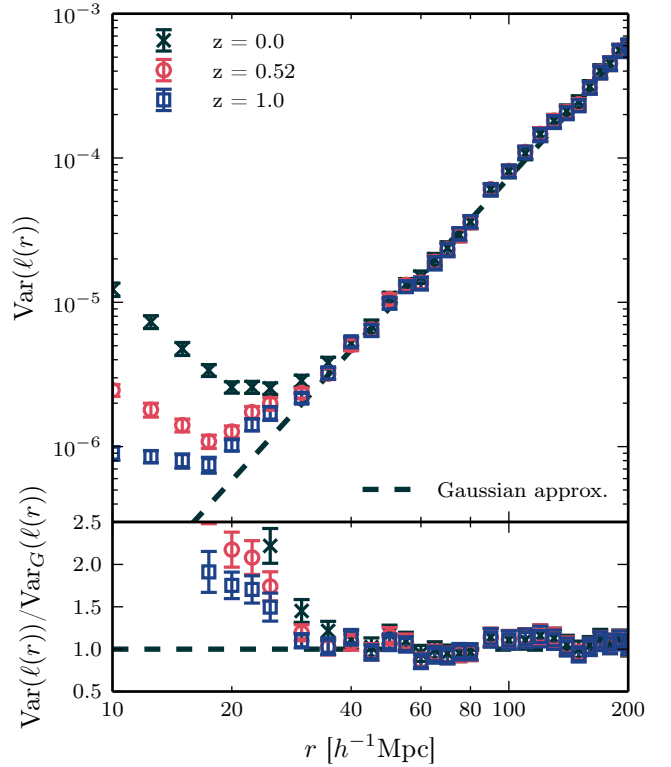


**Figure 5.** Variance of the LCF estimator compared to the Gaussian approximation  $\text{Var}_G(\ell(r))$  from Eq. (42) for the same three redshifts as in Fig. 3. Error bars originate from a Jackknife resampling of the 200 realizations.

From the figure we learn that on large scales higher-order variance terms are clearly negligible and the measured variance displays the expected  $r^3$ -scaling of the Gaussian approximation (Eq. 42). However, at a scale of  $\sim 30 h^{-1}\text{Mpc}$  this agreement breaks down, the variance reaches a minimum and starts increasing with declining scales, which marks the onset of higher-order corrections. While the Gaussian variance is independent of redshift, higher-order terms are not and thus higher redshifts show smaller deviations from the Gaussian approximation. The scale at which the higher-order terms become important coincides with the scale where the measured signal-to-noise was observed to flatten out in Sec. 4.3 but also with the point at which tree-level SPT breaks down (cf. Fig. 3).

Figure 6 shows the full auto- and cross-correlation matrices for the power spectrum (bottom left panel) and LCF (top right panel), where the correlation coefficient  $r_{ij}$  is defined to be:

$$r_{ij} = \frac{\langle \delta X_i \delta X_j \rangle}{\sqrt{\langle \delta X_i^2 \rangle \langle \delta X_j^2 \rangle}}. \quad (64)$$

The figure presents the measurements from simulations as all of the bins below the diagonal, whereas all bins above denote the theoretical prediction from the respective lowest order contributions. In the case of the prediction for the cross-correlation (top left quadrant) this results from the bispectrum term in Eq. (50), computed at tree-level in SPT.

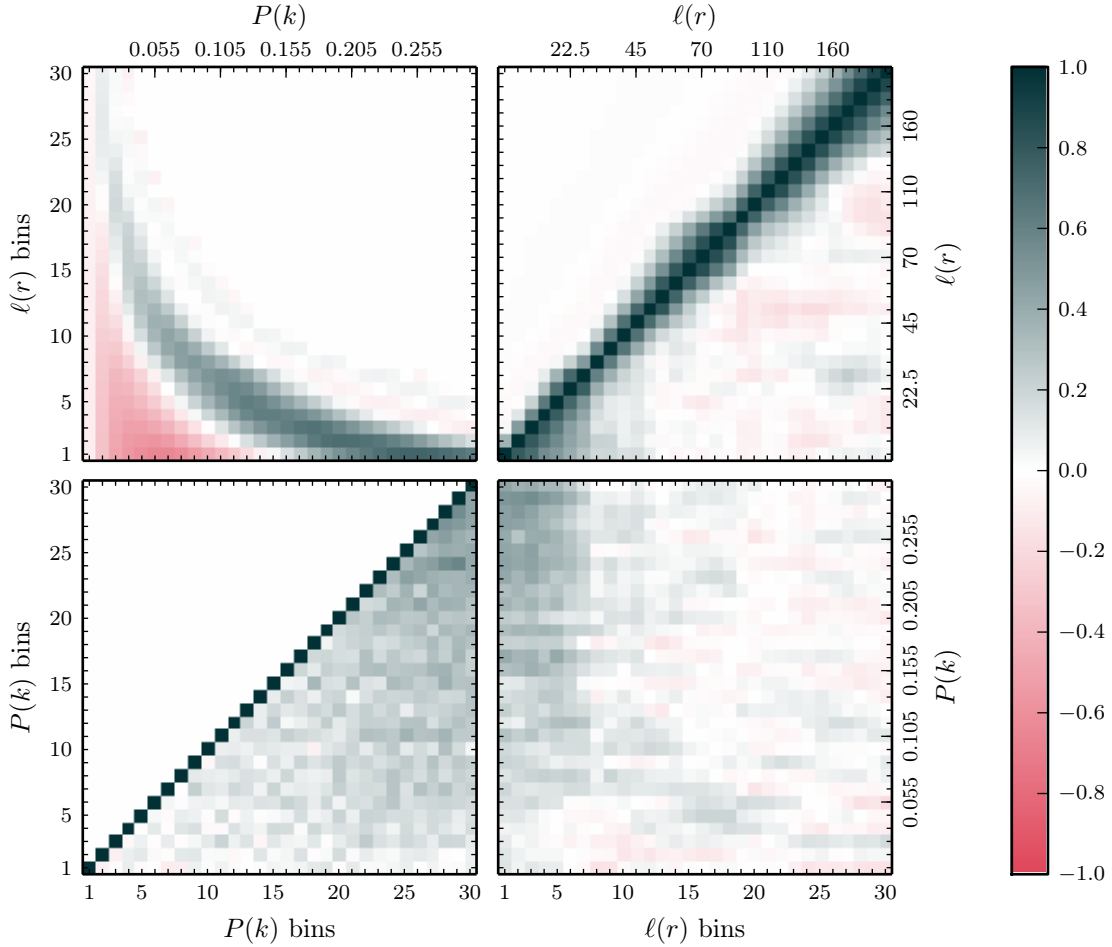


**Figure 6.** Correlation matrices at redshift  $z = 0$  with the auto-correlation of the LCF in the bottom left and the power spectrum in the top right panel. All bins below the diagonal derive from the measurements, all bins above are predictions based on the lowest order contributions to either the auto- or cross-covariance and linear perturbation theory. Note that on power spectrum axes smaller scales (higher  $k$ ) are to the right, whereas for the LCF these lie on the left.

Apart from some noise in the measurements we notice that both auto-correlation matrices are very well reproduced by their Gaussian approximations on large scales. On smaller scales, though, different bins become increasingly correlated with each other, which is underpredicted by the lowest order contributions.

The measured cross-correlation matrix (bottom right quadrant) indicates that the power spectrum and LCF are largely but not entirely independent of each other. The small scale LCF bins seem to be reasonably correlated with most of the power spectrum bins. A qualitatively similar behaviour can be seen from the theoretical computation in the top left quadrant, which displays an arc with moderate correlations for power spectrum and LCF bins that are related by  $k = \pi/r$ . On large scales these correlations are of the order  $\sim 0.2$  and are therefore only hardly identifiable in the measured data, but we do recognize positive correlations along the position of the arc. For small LCF scales and small power spectrum modes the cross-correlation is predicted to become negative, which is not seen in the data. However, in this regime we have to expect the breakdown of tree-level SPT as well as the influence of the next order term in Eq. (50).

## 5 DETECTABILITY OF THE LCF IN FUTURE SURVEYS

### 5.1 Detectability of the LCF in galaxy survey data

Before we move on to discuss the LCF’s sensitivity on various cosmological parameters, we consider the significance at which the LCF might be detected in a hypothetical galaxy survey. Taking the null hypothesis to be the absence of any signal, the  $\chi^2$  of a detection is simply given by

$$\chi_\ell^2 = \sum_{i,j=1}^{N_{\text{bin}}} \hat{\ell}_i \hat{C}_{ij}^{-1} \hat{\ell}_j. \quad (65)$$

Using all 30 bins of our measurements we obtain  $\chi_\ell^2 \approx 10^4$ , where we have accounted for the fact that the inverse of the estimated covariance matrix is not an unbiased estimate of the inverse and applied the Anderson–Hartlap factor (Hartlap et al. 2007), such that

$$\hat{C}^{-1} = \frac{N_{\text{real}} - N_{\text{bin}} - 2}{N_{\text{real}} - 1} \hat{C}_*^{-1}, \quad (66)$$

where  $\hat{C}_*^{-1}$  is the algebraic inverse of the measured covariance matrix. The  $\chi^2$  above is the expected value for a mea-

surement from a single simulation box, which has a volume of  $V_{\text{box}} = (1.5 h^{-1} \text{Gpc})^3$ . As the errors scale inversely with volume, the  $\chi^2_\ell$  for a survey of volume  $V$  and an ideal box-like geometry is thus

$$\chi^2_\ell(V) = 10^4 \frac{V}{V_{\text{box}}}. \quad (67)$$

A  $5\text{-}\sigma$  detection from 30 data points corresponds to a  $\chi^2 \sim 85$  and this could already be achieved by a survey with volume  $V \approx 0.03 h^{-3} \text{Gpc}^3$ .

## 5.2 Detectability of BAO features in the LCF

As was noted in previous plots (e.g. see Figs 1 and 3), the LCF signal displays slight wiggles. These are due to BAO imprinted in the matter distribution (for a review of the physics of BAO see Weinberg et al. 2013). It is therefore interesting to ask: what size does our idealized survey need to be in order to detect these features at a given confidence level? To answer this question we compute again the LCF in tree-level SPT, but this time for a featureless input power spectrum, obtained using the no-wiggle fitting formula of Eisenstein & Hu (1998). The relative difference  $[\hat{\ell}(r) - \ell_{\text{nw}}(r)] / \ell_{\text{nw}}(r)$  between the measured and the no-wiggle LCF enables us to isolate the BAO features more clearly.

Figure 7 shows the results of this operation for our theoretical predictions from SPT (solid black line) and our measurements from simulations (crosses). The shape of this function can be understood as follows, the BAO signal in the two-point function has a local maximum at roughly  $r \sim 100 h^{-1} \text{Mpc}$ , which is an imprint of the sound horizon scale at recombination. Considering the LCF, this correlates three points along a line, each separated by distance  $r$ , and so there appears two values of  $r$  that would produce a resonance with the BAO scale: one when  $r \sim 50 h^{-1} \text{Mpc}$  (i.e. the distance between points 3 and 1) and the second when  $r \sim 100 h^{-1} \text{Mpc}$  (i.e. the separation between points 2 and 1).

Analogously to the procedure of the previous subsection, let us take the standpoint that the no-wiggle LCF represents the null-hypothesis. Hence the  $\chi^2$  for detecting the BAO features can be written:

$$\chi^2_{\text{BAO}} = \sum_{i,j=1}^{N_{\text{bin}}} [\hat{\ell}_i - \ell_{\text{nw}}(r_i)] \hat{\mathbf{C}}_{ij}^{-1} [\hat{\ell}_j - \ell_{\text{nw}}(r_j)]. \quad (68)$$

Taking all 21 bins in the range from 40 to  $200 h^{-1} \text{Mpc}$  we get  $\chi^2_{\text{BAO}} \approx 3.9$ . Requiring a  $3\text{-}\sigma$  confidence level ( $\chi^2 \approx 44$  for 21 data points), this translates into a minimal survey volume of  $V \sim 38 h^{-3} \text{Gpc}^3$ . This is within reach of upcoming galaxy surveys like DES, and certainly the Stage IV dark energy missions such as Euclid and LSST.

## 6 COSMOLOGICAL INFORMATION

We now turn to address the question of the cosmological information content of the LCF, where the principal aim is to unveil which parameters or combination of parameters are best constrained by the LCF and also how it may help to tighten existing constraints obtained from the combination of the galaxy power spectrum and a Planck-like

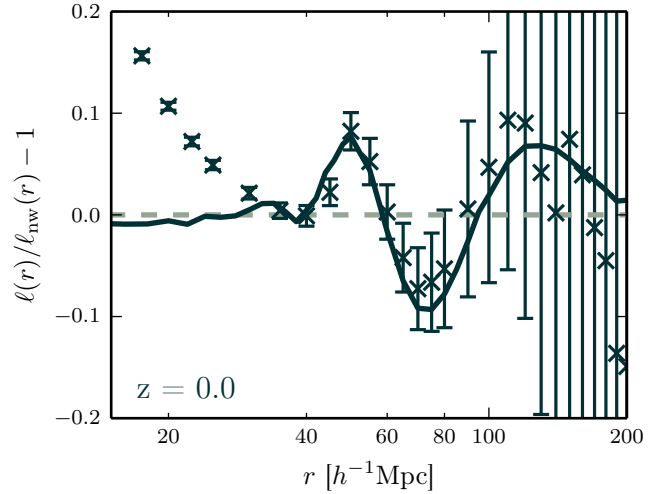


**Figure 7.** Relative difference between measured and no-wiggle LCF, obtained from tree-level perturbation theory and a featureless power spectrum at redshift  $z = 0.0$ . The solid line represents the overall tree-level prediction. Error bars are scaled to match a survey of  $V = 38 h^{-3} \text{Gpc}^3$ .

CMB measurement. Note that our main intention here is not to produce forecasts for a particular survey, but simply to provide a generic assessment of the possible relative gains from measuring the LCF. Thus in what follows we will make various simplifying assumptions. In particular, we will neglect all effects that lead to anisotropies in the clustering of galaxies, such as redshift space distortions and the Alcock-Paczynski effect. Furthermore, we do not take any specifics of the galaxy population being surveyed into account and simply assume an ideal box-like geometry with a constant galaxy number density throughout. However, where possible we will try to add some validation for the choices that we make.

### 6.1 Formalism and assumptions

To begin we assume that the joint likelihood function for both the LCF and the power spectrum takes the form of a multi-variate Gaussian:

$$\mathcal{L} = \frac{1}{\sqrt{(2\pi)^n |\mathbf{C}|}} \exp \left[ -\frac{1}{2} (\mathbf{x} - \boldsymbol{\mu})^T \mathbf{C}^{-1} (\mathbf{x} - \boldsymbol{\mu}) \right], \quad (69)$$

where  $\mathbf{x}$  is the vector containing the measured data, i.e.  $\mathbf{x}^T = \{\hat{P}_1, \dots, \hat{P}_m, \hat{\ell}_1, \dots, \hat{\ell}_n\}$  with mean  $\boldsymbol{\mu} = \langle \mathbf{x} \rangle$ , and  $\mathbf{C}$  is the measured covariance matrix of dimension  $(m+n) \times (m+n)$ . Takahashi et al. (2009) have shown that the probability distribution of the power spectrum estimator is indeed very well approximated by a Gaussian distribution, over a broad range of scales.

For the case of the LCF there are no measurements in the literature to guide us, we therefore use our 200 realizations to determine the LCF probability distribution at four different scales, from 10 to  $100 h^{-1} \text{Mpc}$ . Figure 8 shows the results from these set of measurements. The distribution is plotted as a function of  $\delta\ell = \hat{\ell}_i - \langle \hat{\ell}_i \rangle$ , normalized by the measured standard deviation, such that it should approach a Gaussian distribution with zero mean and unit variance

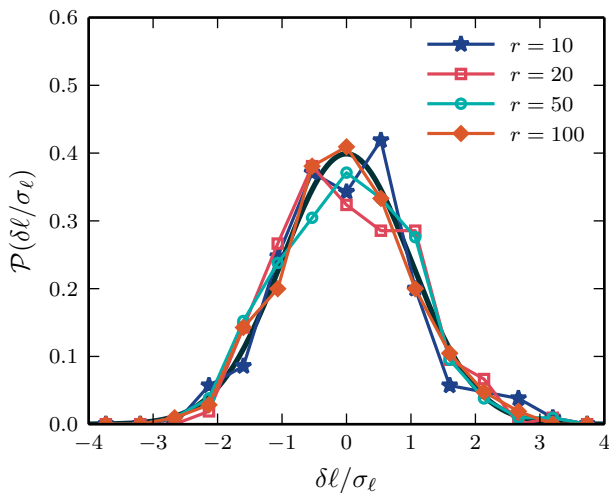


**Figure 8.** Probability distribution of LCF estimator at redshift  $z = 0.0$  as a function of the difference  $\delta\ell = \hat{\ell}_i - \langle \hat{\ell}_i \rangle$ , normalized by the standard deviation. Plotted are the results for various scales (given in units of  $h^{-1}\text{Mpc}$ ) and a Gaussian with zero mean and unit variance (black line) for reference.

(plotted as the thick, black line for reference). Albeit there is some scatter due to the small sample size, we do not observe any significant indication for a strong skewness or kurtosis and thus conclude that for our purposes here, the assumption of a Gaussian likelihood seems justified.

The parameter sensitivity of any statistic can be conveniently forecasted in the Fisher formalism. The Fisher matrix is obtained from the logarithm of the likelihood function by taking second derivatives with respect to the parameters of interest  $\theta_i$ ,

$$F_{ij} = - \left\langle \frac{\partial^2 \log \mathcal{L}}{\partial \theta_i \partial \theta_j} \right\rangle_{\theta=\theta_0}, \quad (70)$$

where  $\theta_0$  denotes the set of fiducial parameter values. In particular, if the likelihood is Gaussian as in Eq. (69), it can be shown that the Fisher matrix takes the form (Tegmark et al. 1997)

$$F_{ij} = \frac{1}{2} \text{Tr} \left[ \mathbf{C}^{-1} \frac{\partial \mathbf{C}}{\partial \theta_i} \mathbf{C}^{-1} \frac{\partial \mathbf{C}}{\partial \theta_j} \right] + \frac{\partial \boldsymbol{\mu}^t}{\partial \theta_i} \mathbf{C}^{-1} \frac{\partial \boldsymbol{\mu}}{\partial \theta_j}. \quad (71)$$

By computing Eq. (71) and then taking the inverse we get the minimal achievable error on a given parameter after marginalizing over all others,

$$\sigma(\theta_i) = \sqrt{(\mathbf{F}^{-1})_{ii}}. \quad (72)$$

To facilitate the evaluation of Eq. (71) we can make a further approximation by neglecting the first term involving derivatives of the covariance matrix. For the case of the power spectrum one can argue that the second term on the right-hand-side of Eq. (71) scales directly with the number of Fourier modes, whereas the first term is independent and consequently is subdominant (Tegmark et al. 1997; Smith et al. 2014). For the case of the LCF this term vanishes identically at lowest order, since, as was shown earlier in Eq. (37), the Gaussian part of the covariance is independent of cosmology and as was demonstrated in Fig. 5 the Gaussian part was shown to be a reasonable approximation for a wide range of scales.

**Table 1.** Fiducial values of the cosmological parameters, along with the stepsizes  $\Delta$  each parameter has been varied in either direction in the simulations. The bias parameters are assumed to be  $b_1 = 1$  and  $b_2 = 0$ .

Param.	$\Omega_m$	$\Omega_b$	$w_0$	$w_a$	$\sigma_8$	$n_s$	$h$
<b>Fid.</b>	0.25	0.040	-1.0	0.0	0.8	1.00	0.70
<b><math>\Delta</math></b>	$\pm 0.05$	$\pm 0.005$	$\pm 0.2$	$\pm 0.1$	$\pm 0.1$	$\pm 0.05$	$\pm 0.05$

## 6.2 Parameter sensitivity

In the following we consider a set of nine parameters,

$$\boldsymbol{\theta} = \{\Omega_m, \Omega_b, w_0, w_a, \sigma_8, n_s, h, b_1, b_2\}, \quad (73)$$

comprising the total matter and baryon densities  $\Omega_m$ ,  $\Omega_b$ , the dark energy equation of state parameters  $w_0$  and  $w_a$ , the amplitude of density fluctuations in spheres of  $8 h^{-1}\text{Mpc}$ , the scalar spectral index  $n_s$  and the dimensionless Hubble rate  $h$ . Lastly, we also include the two bias parameters  $b_1$  and  $b_2$ , using the local Lagrangian bias model introduced in Sec. 2.3. The fiducial values that we are adopting for each of the parameters are summarized in Table 1.

In order to compute the Fisher matrix, we now need to determine how the power spectrum and LCF respond to changes in these parameters, that is we need to evaluate the respective derivatives. To do that, we first generate modified linear power spectra where one of the parameters has been changed by a step up or down according to the values given in Table 1, while all others are kept at the fiducial value. Using these spectra we compute the LCF in the tree-level approximation of Eq. (12) and additionally all one-loop power spectra. That is necessary in order to include the bias parameter  $b_2$  in the power spectrum Fisher matrix because at linear order it only depends on  $b_1$ . The corrections due to non-linear and non-local bias terms are summarized in App. B. The derivatives are finally obtained by taking the central finite difference of the upward and downward steps, i.e.

$$\frac{dX_i(\boldsymbol{\theta})}{d\theta_\alpha} \approx \frac{X_i(\boldsymbol{\theta} + \Delta\theta_\alpha) - X_i(\boldsymbol{\theta} - \Delta\theta_\alpha)}{2\Delta\theta_\alpha}, \quad (74)$$

whereas for the two bias parameters we calculate the exact derivatives from Eqs. (16) and (B1).

To check the accuracy of these model predictions, we also measure the derivatives directly from a set of simulations whose cosmological parameters are varied in the same way as the ones given in Table 1 (originally performed in Smith et al. 2014). The specifics of the simulations are the same as the ones described in Sec. 4.1 and for each variation as well as the fiducial parameter set there are four realizations. To reduce the effect from sample variance, the phases of the initial Gaussian random field of each realization are matched to the corresponding one from the fiducial model. Derivatives are estimated as in Eq. (74) and averaged over the four realizations.

Figure 9 shows the comparison of our predictions for the logarithmic derivatives (depicted by solid lines) with the measurements from the  $N$ -body simulations (circles and crosses), and for the various cosmological models considered. The left panel shows the derivatives of the power spectrum and the right the LCF. In the left panel of Fig. 9 we see that the power spectrum derivatives are reasonably well captured

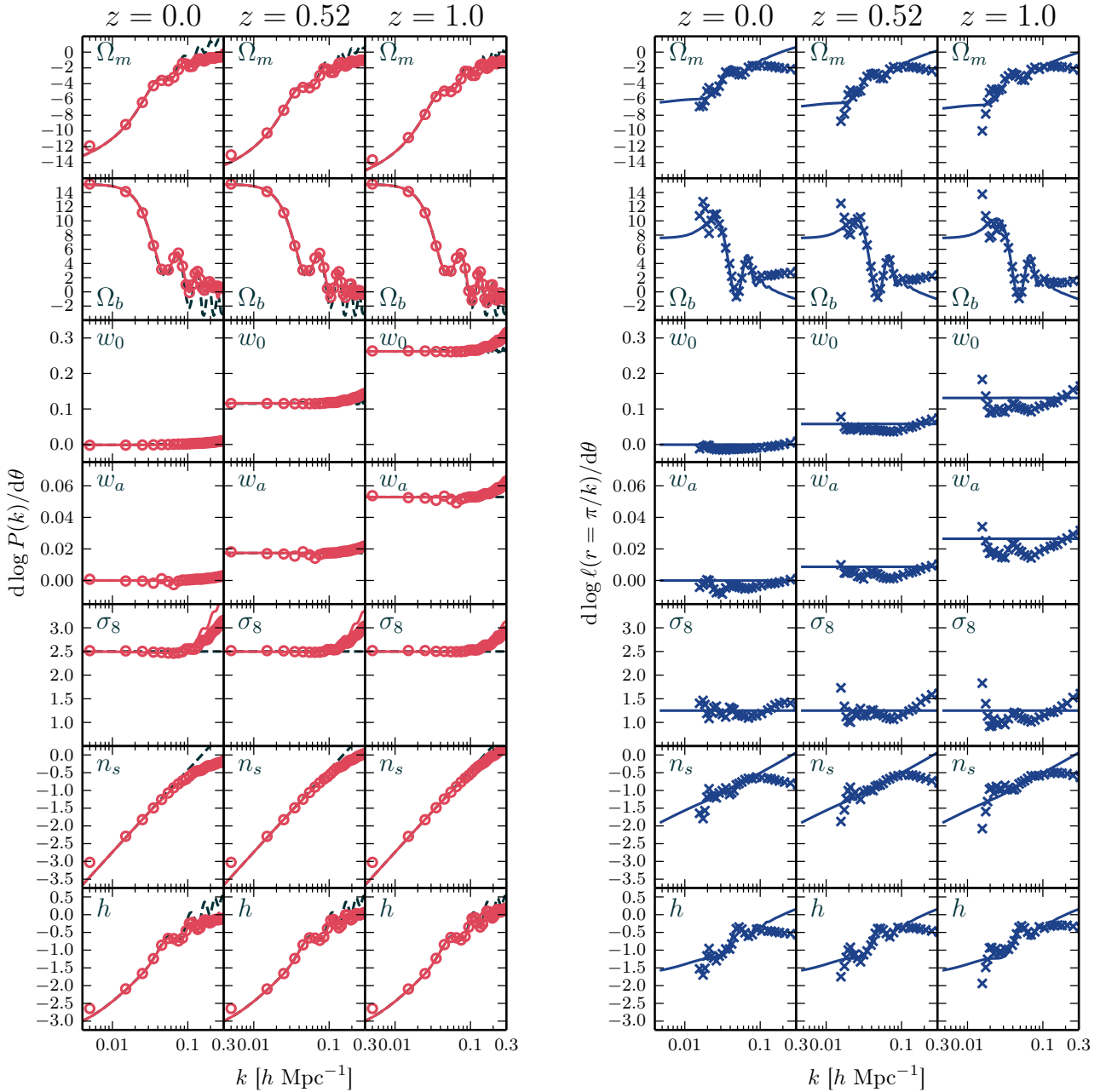


**Figure 9.** Time evolution of the logarithmic derivatives of power spectrum (left) and LCF (right) with respect to various cosmological parameters. Data points represent direct measurements from the N-body simulations described in the text, while solid lines are the respective model predictions. For comparison, in the left panel we also show the linear power spectrum derivatives as the black, dashed lines.

by the one-loop model up to the maximal scale that is being considered,  $k = 0.3 h \text{ Mpc}^{-1}$ . Note that for reference we also show the linear theory derivatives, indicated as the dashed lines. Considering the right panel of Fig. 9 we see that the tree-level predictions for the LCF are in reasonable agreement with the simulations up to  $k = 0.1 h \text{ Mpc}^{-1}$ , beyond which the measured data display, in absolute terms, a larger derivative than the one predicted.

On comparing the power spectrum derivatives with those of the LCF, we find that the former usually dominate over the latter. For the three parameters  $w_0$ ,  $w_a$  and  $\sigma_8$ , which mainly affect the amplitude of the power spec-

trum, the difference is a factor of  $\sim 2$  over the scales considered. This matches our expectations, since as may be noted from inspecting Eq. (12) the LCF scales with the square root of the power spectrum amplitude. On the other hand, for the remaining four parameters we find that the power spectrum derivatives are only larger than the LCF ones on very large scales. On smaller scales the derivatives approach zero, signalling that the power spectrum does not provide much information on these parameters in the non-linear regime. The LCF model also predicts nearly vanishing derivatives on small scales but the fully non-linear measurements all

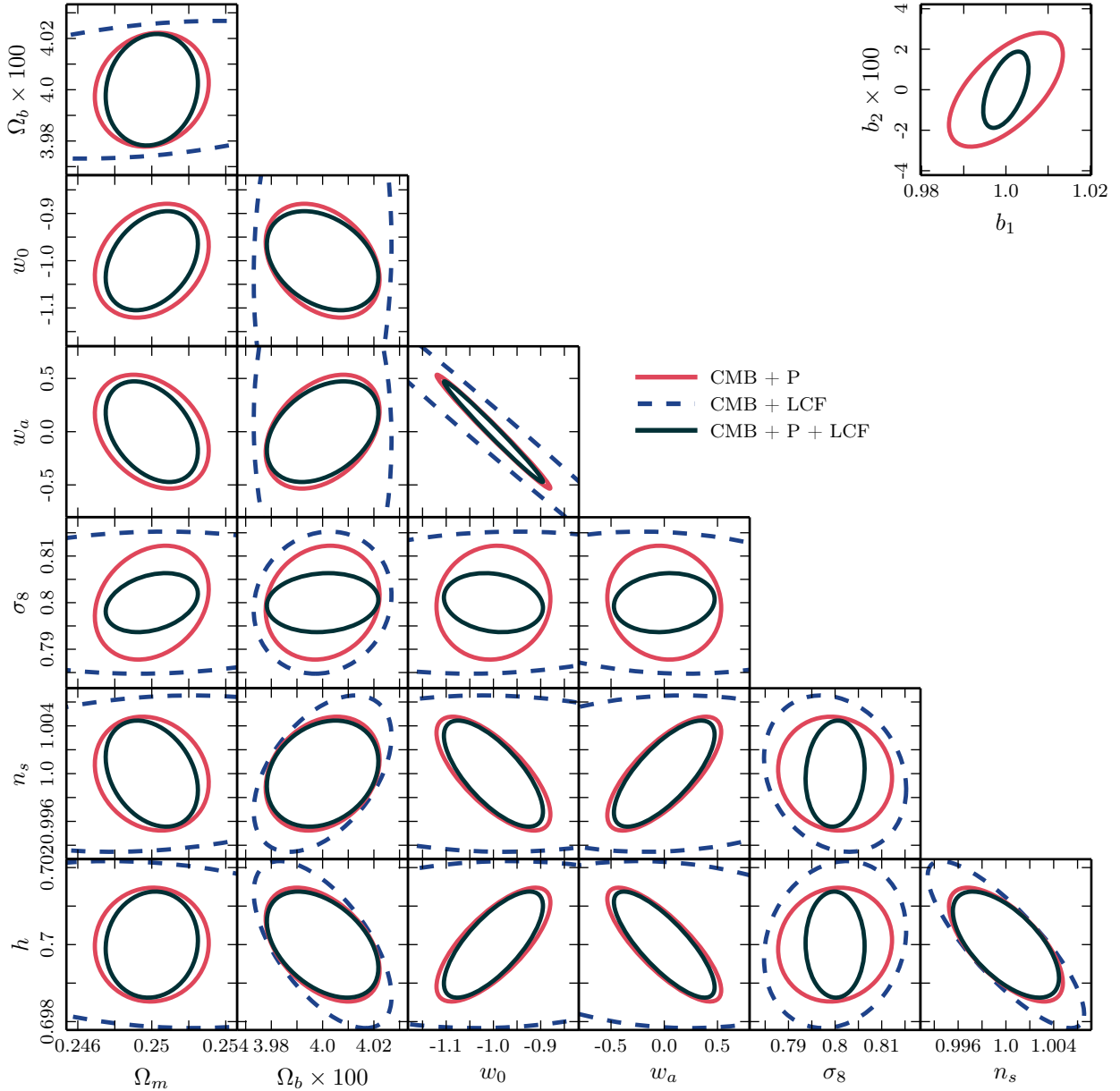


**Figure 10.** Forecasted  $1\text{-}\sigma$  likelihood contours for various combinations of parameters, marginalized over all others. Power spectrum forecasts are represented by the red lines, the LCF by the blue dashed ones and their combination is shown in black. All forecasts use a cutoff scale  $k_{\text{max}} = 0.3 h \text{ Mpc}^{-1}$  (corresponding to  $r_{\text{min}} \sim 10 h^{-1} \text{ Mpc}$ ) and include information from a *Planck*-like CMB experiment.

saturate at some value, such that it is still possible to gain some information.

### 6.3 Forecasted parameter accuracy

To compute the Fisher matrix we assume that our idealistic survey consists of three independent redshift slices at  $z = 0.0, 0.52$  and  $1.0$ , each of a volume  $V = 3.375 (h^{-1} \text{ Gpc})^3$ , so that the total Fisher matrix based on large-scale structure is given by

$$\mathbf{F}^{\text{LSS}} = \mathbf{F}(z = 0.0) + \mathbf{F}(z = 0.52) + \mathbf{F}(z = 1.0). \quad (75)$$

We take the theory predictions presented in Sec. 6.2 to model the parameter derivatives but use the fully non-linear covariance matrices estimated from the large suite of N-body sim-

ulations and correct the inverse for the Anderson–Hartlap factor (see Sec. 5). When considering combinations of power spectrum and LCF we use a bit more caution when calculating the inverse as the two statistics have signals of widely differing orders of magnitudes. Consequently, the entries in the combined covariance matrix will equally vary by large amounts, making the inversion process subject to numerical errors. For that reason we first compute the correlation matrix  $\mathbf{r}$ , whose entries all lie in the interval  $[-1, 1]$ , and obtain its inverse via a singular value decomposition. The (uncorrected) inverse of the covariance matrix can then be written as (Smith et al. 2014)

$$\mathbf{C}_{*,ij}^{-1} = \frac{r_{*,ij}^{-1}}{\sigma_i \sigma_j}. \quad (76)$$



**Table 2.** Marginalized  $1\text{-}\sigma$  errors for power spectrum and a combination of power spectrum and LCF (CMB priors are included in all cases). The first four columns use the cutoff scale  $k_{\text{max}} = 0.2 h \text{Mpc}^{-1}$  ( $r_{\text{min}} \sim 16 h^{-1} \text{Mpc}$ ), the last four  $k_{\text{max}} = 0.3 h \text{Mpc}^{-1}$  ( $r_{\text{min}} \sim 10 h^{-1} \text{Mpc}$ ). Two columns for each cutoff scale correspond to the case where the two bias parameters have been fixed to their fiducial values. The percentages in the parenthesis indicate the improvement over the respective power spectrum results.

	P	P + LCF	P	P + LCF	P	P + LCF	P	P + LCF
	$k_{\text{max}} = 0.2 h \text{Mpc}^{-1}$		fixed bias		$k_{\text{max}} = 0.3 h \text{Mpc}^{-1}$		fixed bias	
$\Delta\Omega_m$	0.0022	0.0019 (14%)	0.0016	0.0015 (4%)	0.0020	0.0016 (19%)	0.00122	0.00116 (5%)
$\Delta\Omega_b$	0.000153	0.000151 (1%)	0.000151	0.000150 (1%)	0.000146	0.000143 (2%)	0.000145	0.000142 (2%)
$\Delta w_0$	0.094	0.084 (11%)	0.088	0.083 (6%)	0.079	0.069 (13%)	0.078	0.069 (12%)
$\Delta w_a$	0.401	0.370 (8%)	0.388	0.369 (5%)	0.352	0.311 (12%)	0.347	0.311 (10%)
$\Delta\sigma_8$	0.0096	0.0060 (38%)	0.0012	0.0011 (9%)	0.0080	0.0042 (48%)	0.0010	0.0008 (21%)
$\Delta n_s$	0.0035	0.0033 (4%)	0.0034	0.0033 (1%)	0.0031	0.0029 (7%)	0.0030	0.0029 (4%)
$\Delta h$	0.00109	0.00106 (3%)	0.00108	0.00106 (2%)	0.00097	0.00091 (7%)	0.00095	0.00090 (5%)
$\Delta b_1$	0.012	0.005 (60%)	–	–	0.009	0.004 (60%)	–	–
$\Delta b_2$	0.023	0.020 (13%)	–	–	0.018	0.012 (33%)	–	–

Furthermore, we add the information coming from a CMB experiment like *Planck*, acting as priors for our parameter set. For that we initially compute the CMB Fisher matrix in a different parameter set that is more suitable for the CMB and then transform this matrix to match our chosen large-scale structure parameters (for more details, see App. A of [Smith et al. 2014](#)). We treat the CMB information as independent from the large-scale structure and hence the total Fisher matrix is finally given by

$$\mathbf{F}^{\text{tot}} = \mathbf{F}^{\text{LSS}} + \mathbf{F}^{\text{CMB}}. \quad (77)$$

Figure 10 shows the  $1\text{-}\sigma$  likelihood contours derived from this Fisher matrix for various combinations of parameters, after marginalizing over all others, and a maximal mode  $k_{\text{max}} = 0.3 h \text{Mpc}^{-1}$  ( $r_{\text{min}} \sim 10 h^{-1} \text{Mpc}$ ). The error ellipses are constructed by inverting  $\mathbf{F}^{\text{tot}}$  and reducing it to a  $2 \times 2$  submatrix of the desired parameters. This submatrix is inverted back again and we determine its eigenvalues and eigenvectors, which are used as input to plot the corresponding error ellipses. In each panel the red lines represent the case where  $\mathbf{F}^{\text{LSS}}$  is evaluated for the power spectrum alone, the blue dashed lines are for the LCF and the black ones the combination of both measures. Note that the CMB prior is always added.

The figure illustrates that there are some substantial gains over the power spectrum plus CMB alone to be made. In particular, the largest gains are obtained for the  $\sigma_8$  parameter, which is mainly a proxy for the amplitude of fluctuations, and the two bias parameters  $b_1$  and  $b_2$ . There is also a more modest improvement in the constraints on the matter density parameter  $\Omega_m$ . However, for the other parameters  $\{\Omega_b, n_s, h, w_0, w_a\}$  the gains are marginal. For the first three parameters, this is not too surprising since they are already well constrained by the CMB. The dark energy equation of state parameters do not display a significant improvement, either. Perhaps this owes to the fact that the LCF is only very weakly dependent on growth history and the nonlinear interaction kernel seems to be somewhat cosmology independent.

The above qualitative findings are shown more quantitatively in Table 2, which summarizes the marginalized  $1\text{-}\sigma$  errors for all parameters and for two different cutoff scales: the one used for Fig. 10 as well as the more conservative choice  $k_{\text{max}} = 0.2 h \text{Mpc}^{-1}$ . The combinations of power spec-

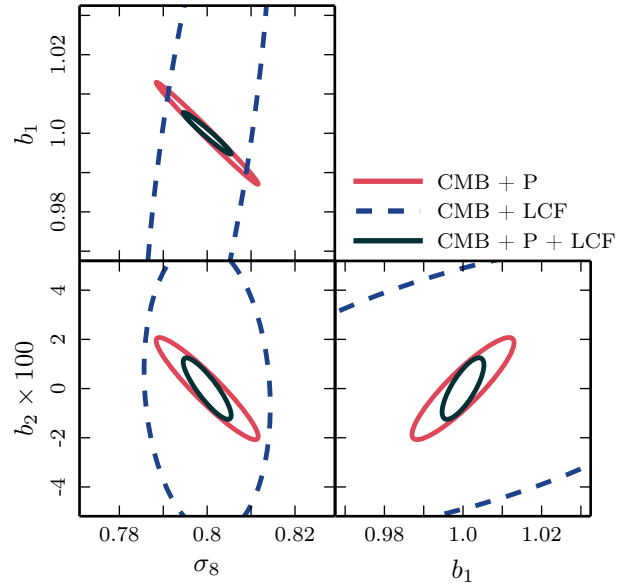


**Figure 11.** Forecasted  $1\text{-}\sigma$  likelihood contours as in Fig. 10 but for a subset of parameters including  $\sigma_8$ ,  $b_1$  and  $b_2$ . The cutoff scale is chosen to be  $k_{\text{max}} = 0.3 h \text{Mpc}^{-1}$ .

trum and LCF (including the CMB priors) are to be found in the sixth and second data column, respectively, where the percentages in parenthesis give the improvement compared to the power spectrum alone and we read off that the errors for  $\sigma_8$  and  $b_1$  decrease by 48 and even 60% when LCF information is included. Interestingly, we obtain comparable improvement factors when the lower cutoff is being used, only  $b_2$  displays a larger change from 13 to 33%, indicating that the information coming from smaller LCF scales are particularly helpful in constraining non-linear bias. However, we note that the improvement factors are slightly underestimated because as we have seen in Sec. 6.2, our LCF model somewhat underpredicts the parameter sensitivity in the non-linear regime.

We also consider the case where we assume that the bias parameters are known and fixed to their fiducial values, meaning that we simply strike out all the corresponding rows and columns in  $\mathbf{F}^{\text{tot}}$ . The resulting errors are given in the last two columns for each cutoff scale and we now observe

a reduction of all improvement factors, which is particularly evident for  $\Omega_m$  and  $\sigma_8$ . That implies that for these parameters the gain from the LCF is mainly due to a better constraint of galaxy bias. We also see that the inclusion of a larger amount of the small scale modes now brings about slightly more significant improvements.

To further investigate where the main constraining power of the LCF is coming from, we analyze a subset of our parameters that just comprises  $\sigma_8$  and the bias parameters. The resulting likelihood contours of an analogue Fisher matrix computation are shown in Fig. 11 and they clarify why we obtain the comparably good improvements noted above. Even though the LCF cannot put a tight constraint on  $b_1$ , it does produce small error bars for  $\sigma_8$  (cf.  $\Delta\sigma_8$  in the last column of Table 2). As the degeneracy direction in the  $\sigma_8$ - $b_1$  plane (see top left panel in Fig. 11) for the LCF is fundamentally different from that of the power spectrum, a combination of both measures lead to good constraints, which in turn carry over to  $b_2$ . This behaviour is reasonable because as was shown in Sec. 2.3 the LCF is independent of linear bias at lowest order (but not of  $\sigma_8$ ) and thus breaks the degeneracy between both parameters when combined with e.g. the power spectrum.

## 7 DISCUSSION AND CONCLUSIONS

In this paper, we have studied the ability of the LCF to constrain the cosmological model in combination with power spectra measurements of the large-scale galaxy and CMB fluctuations.

In order to achieve this it was necessary to extend the LCF from describing matter fluctuations to those of galaxy fluctuations. In §2 we did this by computing the LCF in the Lagrangian biasing scheme. While the LCF is independent of bias in the regime where the relation between the galaxy and dark matter overdensities is linear, we have seen that non-linearity and non-locality introduce additional terms. However, if bias is assumed to be local in Lagrangian space (this approach was adopted in recent bispectrum measurements from BOSS by Gil-Marín et al. 2016), the LCF still breaks the degeneracy between the amplitude of density fluctuations and the two remaining bias parameters. In comparison, this is not possible if one considers the bispectrum alone.

We also determined the effect of shot noise on the LCF, finding that after additive contributions are removed the signal becomes increasingly suppressed with decreasing number densities. Unlike more conventional clustering measures, the LCF cannot be completely cleaned from shot noise and the galaxy number density must hence be incorporated into the modelling.

In §3 we provided the first ever derivation of the LCF auto-covariance and its cross-covariance with the power spectrum. We noted that there was a structural similarity for the joint covariance we computed and that associated with the joint covariance between the power spectrum and the bispectrum. More importantly, though, we were able to prove that, in the Gaussian limit, the lowest order contribution to the LCF covariance was independent of cosmological parameters. For that reason it is not subject to non-linear evolution and can therefore be predicted exactly. This property might prove to be advantageous compared to the

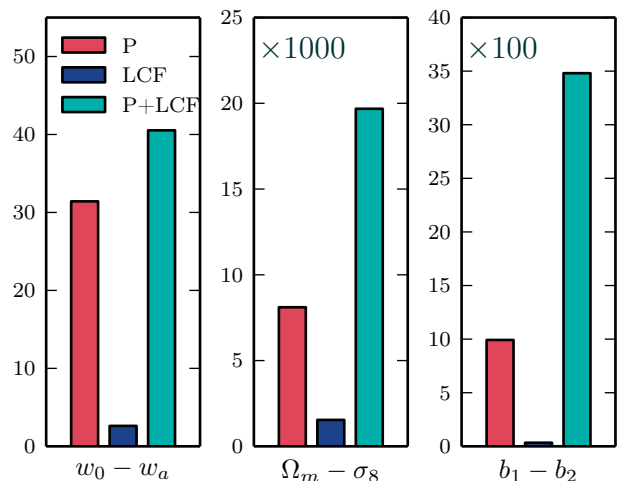


**Figure 12.** Figure of merit for three different parameter combinations. The bar on the left in each panel is the power spectrum, the middle bar marks the LCF and the last one the combination of both. All three include the CMB priors.

bispectrum, as it might allow us to produce accurate covariance matrices from relatively cheap small-scale  $N$ -body simulations, matched with the analytic results in the Gaussian limit. Of course there are additional higher order corrections which involve the trispectrum, quadratic powers of the bispectrum, and the 6-point spectrum of the phase field that could complicate this possibility.

In §4 we confronted our analytic results with measurements from a large ensemble of  $N$ -body simulations, comprising a total combined volume of  $675 h^{-3} \text{Gpc}^3$ . The simulations enabled us to produce the first ever measurement of the LCF at the BAO scale, with enough volume, to unambiguously detect the acoustic oscillation features. Through the simulation to simulation variance, we were also able to produce the first ever measurement of the LCF covariance matrix and its cross-covariance with the power spectrum. We found that the Gaussian approximation of the covariance holds down to scales  $\sim 40 h^{-1} \text{Mpc}$ , slightly above the scale where the tree-level SPT result for the LCF breaks down. As expected, the power spectrum and LCF are mostly uncorrelated but we do detect moderate correlations of the order  $\lesssim 0.4$  for small LCF bins as well as bins of equivalent scales, i.e. those, which are related via  $k \approx \pi/r$ .

In addition, we also computed the signal-to-noise ratio of the LCF, from which we discovered that the power spectrum dominates over the LCF up to  $k_{\text{max}} = 0.3 h \text{Mpc}^{-1}$  ( $\sim 10 h^{-1} \text{Mpc}$ ). However, the LCF signal-to-noise shows a stronger increase with decreasing scale. This suggests that there is potentially more information to be gained in the LCF than the power spectrum by pushing to smaller scales.

In §5 we turned to assessing the detectability of the LCF in galaxy surveys. We found that the LCF could be measured at  $> 5\sigma$  significance in a survey of volume  $V > 0.03 h^{-3} \text{Gpc}^3$  – this paves the way for a very high significance measurement in modern surveys like the SDSS main sample and BOSS. On the other hand, we found that in order to detect the BAO signature one would require a survey that spans a volume of roughly  $V \sim 40 h^{-3} \text{Gpc}^3$  and hence this would only likely

be possible with future Stage IV missions like Euclid and LSST.

In §6 we explored the main question of this paper, which was the cosmological information content of the LCF. We considered a large-scale structure survey of total volume  $\sim 10 h^{-3} \text{Gpc}^3$ , up to  $z \sim 1$  – thus comparable with Stage-III like spectroscopic missions (Albrecht et al. 2006). We found that when estimates of the LCF are combined with estimates of the galaxy power spectrum and a Planck-like CMB experiment, significant improvements may be found in constraints on the amplitude of density fluctuations  $\sigma_8$  (roughly a factor of  $\sim 2$ ) and to more modest improvements in the matter density parameter  $\Omega_m$  ( $\sim 20\%$ ). In addition, one is able to significantly improve constraints on the nonlinear galaxy bias parameters  $b_1$  and  $b_2$  (factor  $\sim 2$ ). Expressed in terms of the figure of merit (see Fig. 12) we obtain improvement factors of  $\sim 3.5$  and  $\sim 2.4$  for the parameter combinations  $b_1$ – $b_2$  and  $\Omega_m$ – $\sigma_8$ , respectively<sup>1</sup>. On the other-hand we find no significant improvement to be gained in the traditional dark energy figure of merit (it changes by a factor of  $\sim 1.3$ ).

As we have only used 30 bins for our forecasts, these results suggest that the LCF provides an efficient compression of higher-order information. This could prove to be advantageous over the bispectrum, as it simplifies the task of generating accurate covariance matrices. Clearly, a more detailed study comparing various higher-order statistics is necessary to make a more definitive statement and will be presented in a forthcoming paper. Besides, by definition the LCF probes a very particular configuration of three points, so it would be interesting to explore whether there are more optimal shapes for constraining parameters.

Finally, to facilitate the Fisher analysis in this paper, we have made a number of simplifications. In particular, we have neglected effects from redshift space distortions; the imprint of the finite survey geometry and survey mask on the phase field. Both of these will need to be explored in future work to arrive at more realistic forecasts and methodology for survey analysis. Accounting for redshift space distortions should provide additional information. Moreover, owing to the fact that in a power spectrum analysis the growth rate of structure  $f(\Omega)$  is strongly degenerate with  $\sigma_8$  and  $b_1$ , we expect the LCF will also prove to be effective in breaking these degeneracies and so *should* provide improvements in the dark energy figure of merit. Furthermore, we have assumed throughout that the primordial density field was Gaussian. If this was not the case, the LCF would acquire a further contribution, whose amplitude  $f_{\text{NL}}$  would be naturally degenerate with  $b_1$ , which means it can be potentially well constrained by a combination of power spectrum and LCF.

<sup>1</sup> The figure of merit is defined as the inverse area enclosed by the  $2\sigma$  error ellipse for any combination of two parameters (Albrecht et al. 2006), i.e.

$$\text{FOM}(\theta_i, \theta_j) \equiv \frac{1}{\pi \sqrt{6.17 \text{Det} [\mathbf{F}^{-1}(\theta_i, \theta_j)]}},$$

where  $\mathbf{F}(\theta_i, \theta_j)$  is the  $2 \times 2$  Fisher matrix of the parameters  $\theta_i$  and  $\theta_j$ .

## ACKNOWLEDGMENTS

We would like to thank Joyce Byun, Donough Regan and David Seery for useful discussions. AE acknowledges support from the STFC for his PhD studentship funding.

## REFERENCES

- Alam S., et al., 2016, preprint, ([arXiv:1607.03155](https://arxiv.org/abs/1607.03155))  
 Albrecht A., et al., 2006, [arXiv:astro-ph/0609591](https://arxiv.org/abs/astro-ph/0609591),  
 Alpaslan M., et al., 2014, [MNRAS](https://doi.org/10.1093/mnras/stt1500), **440**, L106  
 Baldauf T., Seljak U., Desjacques V., McDonald P., 2012, [PRD](https://doi.org/10.1088/1475-2875/201203/001), **86**, 083540  
 Bernardeau F., Colombi S., Gaztañaga E., Scoccimarro R., 2002, [Phys. Rep.](https://doi.org/10.1016/S0370-1571(02)00033-9), **367**, 1  
 Catelan P., Porciani C., Kamionkowski M., 2000, [MNRAS](https://doi.org/10.1046/j.1365-8711.2000.03183.x), **318**, L39  
 Chan K. C., Scoccimarro R., Sheth R. K., 2012, [PRD](https://doi.org/10.1088/1475-2875/201203/001), **85**, 083509  
 Chiang C.-T., Wagner C., Schmidt F., Komatsu E., 2014, [Journal of Cosmology and Astro-Particle Physics](https://doi.org/10.1088/1475-2875/201403/001), **5**, 048  
 Crocce M., Scoccimarro R., 2006, [PRD](https://doi.org/10.1088/1475-2875/200603/001), **73**, 063519  
 Eggemeier A., Battfeld T., Smith R. E., Niemeyer J., 2015, [MNRAS](https://doi.org/10.1093/mnras/stv1500), **453**, 797  
 Eisenstein D. J., Hu W., 1998, [ApJ](https://doi.org/10.1086/3051800), **496**, 605  
 Eisenstein D. J., et al., 2005, [ApJ](https://doi.org/10.1086/4295167), **633**, 560  
 Feldman H. A., Kaiser N., Peacock J. A., 1994, [ApJ](https://doi.org/10.1086/3969797), **426**, 23  
 Fry J. N., 1984, [ApJ](https://doi.org/10.1086/3071997), **279**, 499  
 Fry J. N., 1994, [Physical Review Letters](https://doi.org/10.1103/PhysRevLett.73.215), **73**, 215  
 Fry J. N., Gaztanaga E., 1993, [ApJ](https://doi.org/10.1086/3071997), **413**, 447  
 Gil-Marín H., Percival W. J., Verde L., Brownstein J. R., Chuang C.-H., Kitaura F.-S., Rodríguez-Torres S. A., Olmstead M. D., 2016, preprint, ([arXiv:1606.00439](https://arxiv.org/abs/1606.00439))  
 Hartlap J., Simon P., Schneider P., 2007, [A&A](https://doi.org/10.1051/0004-6361/200710533), **464**, 399  
 Hikage C., Matsubara T., Suto Y., 2004, [ApJ](https://doi.org/10.1086/4295167), **600**, 553  
 Lewis A., Challinor A., Lasenby A., 2000, [ApJ](https://doi.org/10.1086/3071997), **538**, 473  
 Matarrese S., Verde L., Heavens A. F., 1997, [MNRAS](https://doi.org/10.1093/mnras/290.2.651), **290**, 651  
 Matsubara T., 2003, [Astrophys.J.](https://doi.org/10.1086/3791197), **591**, L79  
 Matsubara T., 2006, preprint ([arXiv:astro-ph/0610536](https://arxiv.org/abs/astro-ph/0610536))  
 McDonald P., Roy A., 2009, [Journal of Cosmology and Astro-Particle Physics](https://doi.org/10.1088/1475-2875/200903/001), **8**, 020  
 Munshi D., Heavens A., 2010, [MNRAS](https://doi.org/10.1093/mnras/401.2.2406), **401**, 2406  
 Norberg P., Baugh C. M., Gaztañaga E., Croton D. J., 2009, [MNRAS](https://doi.org/10.1093/mnras/396.1.19), **396**, 19  
 Obreschkow D., Power C., Bruderer M., Bonvin C., 2013, [ApJ](https://doi.org/10.1088/1475-2875/201303/001), **762**  
 Peebles P. J. E., 1980, The large-scale structure of the universe  
 Pollack J. E., Smith R. E., Porciani C., 2014, [MNRAS](https://doi.org/10.1093/mnras/440.2.555), **440**, 555  
 Regan D. M., Schmittfull M. M., Shellard E. P. S., Fergusson J. R., 2012, [PRD](https://doi.org/10.1088/1475-2875/201203/001), **86**, 123524  
 Saito S., Baldauf T., Vlah Z., Seljak U., Okumura T., McDonald P., 2014, [PRD](https://doi.org/10.1088/1475-2875/201403/001), **90**, 123522  
 Schmittfull M., Baldauf T., Seljak U., 2015, [PRD](https://doi.org/10.1088/1475-2875/201503/001), **91**, 043530  
 Sefusatti E., Scoccimarro R., 2005, [PRD](https://doi.org/10.1088/1475-2875/200503/001), **71**, 063001  
 Sefusatti E., Crocce M., Pueblas S., Scoccimarro R., 2006, [PRD](https://doi.org/10.1088/1475-2875/200603/001), **74**, 023522  
 Seljak U., Zaldarriaga M., 1996, [ApJ](https://doi.org/10.1086/3071997), **469**, 437  
 Slepian Z., et al., 2016, preprint, ([arXiv:1607.06097](https://arxiv.org/abs/1607.06097))  
 Smith R. E., 2009, [MNRAS](https://doi.org/10.1093/mnras/400.2.851), **400**, 851  
 Smith R. E., Scoccimarro R., Sheth R. K., 2007, [PRD](https://doi.org/10.1088/1475-2875/200703/001), **75**, 063512  
 Smith R. E., Reed D. S., Potter D., Marian L., Crocce M., Moore B., 2014, [MNRAS](https://doi.org/10.1093/mnras/440.2.249), **440**, 249  
 Springel V., 2005, [MNRAS](https://doi.org/10.1093/mnras/364.2.1105), **364**, 1105  
 Takahashi R., et al., 2009, [ApJ](https://doi.org/10.1086/3791197), **700**, 479  
 Tegmark M., 1997, [Physical Review Letters](https://doi.org/10.1103/PhysRevLett.79.3806), **79**, 3806  
 Tegmark M., Taylor A. N., Heavens A. F., 1997, [ApJ](https://doi.org/10.1086/3071997), **480**, 22  
 Tegmark M., et al., 2006, [PRD](https://doi.org/10.1088/1475-2875/200603/001), **74**, 123507  
 Watts P., Coles P., Melott A., 2003, [ApJL](https://doi.org/10.1088/1475-2875/200303/001), **589**, L61

Weinberg D. H., Mortonson M. J., Eisenstein D. J., Hirata C., Riess A. G., Rozo E., 2013, *Phys. Rep.*, **530**, 87  
 Wolstenhulme R., Bonvin C., Obreschkow D., 2015, *ApJ*, **804**, 132

## APPENDIX A: THE JOINT PROBABILITY DENSITY FUNCTION OF FOURIER MODES

In this appendix we present results from Matsubara (2003, 2006), which will be used for the derivation of the LCF covariance in Sec. 3.

Given a density field enclosed in a box of volume  $V$  with discrete Fourier modes  $\delta_{\mathbf{k}}$ , all of its statistical properties are encoded in the probability density function (PDF)  $\mathcal{P}$ . Normalizing the density modes by volume and their power spectrum we get the dimensionless variables  $\alpha_{\mathbf{k}} \equiv \delta_{\mathbf{k}}/\sqrt{V P(k)}$ , in terms of which the PDF can be written as

$$\mathcal{P}[\alpha_{\mathbf{k}}] = \exp \left[ \sum_{N=3}^{\infty} \frac{(-1)^N}{N!} \sum_{\mathbf{k}_1} \cdots \sum_{\mathbf{k}_N} \langle \alpha_{\mathbf{k}_1} \cdots \alpha_{\mathbf{k}_N} \rangle_c \times \frac{\partial}{\partial \alpha_{\mathbf{k}_1}} \cdots \frac{\partial}{\partial \alpha_{\mathbf{k}_N}} \right] \mathcal{P}_G[\alpha_{\mathbf{k}}], \quad (\text{A1})$$

where

$$\mathcal{P}_G[\alpha_{\mathbf{k}}] = \frac{1}{2\pi} \exp \left( -\frac{1}{2} \sum_{\mathbf{k}} \alpha_{\mathbf{k}} \alpha_{-\mathbf{k}} \right) \quad (\text{A2})$$

denotes the Gaussian PDF. The  $\langle \alpha_{\mathbf{k}_1} \cdots \alpha_{\mathbf{k}_N} \rangle_c$  refer to the  $N$ -th order cumulants,

$$\langle \alpha_{\mathbf{k}_1} \cdots \alpha_{\mathbf{k}_N} \rangle_c = p^{(N)}(\mathbf{k}_1, \dots, \mathbf{k}_N) \delta_{\mathbf{k}_1 + \dots + \mathbf{k}_N}^K, \quad (\text{A3})$$

which are related to normalized (and dimensionless) versions of the ordinary  $N$ -th order spectra  $P^{(N)}$ , defined as

$$p^{(N)}(\mathbf{k}_1, \dots, \mathbf{k}_N) \equiv V^{1-\frac{N}{2}} \frac{P^{(N)}(\mathbf{k}_1, \dots, \mathbf{k}_N)}{\sqrt{P(\mathbf{k}_1) \cdots P(\mathbf{k}_N)}}. \quad (\text{A4})$$

For mildly non-Gaussian fields we can expand the exponential in Eq. (A1),

$$\mathcal{P}[\alpha_{\mathbf{k}}] = \left[ 1 + \sum_{n=1}^{\infty} \mathcal{Q}^{(n)} \right] \mathcal{P}_G[\alpha_{\mathbf{k}}], \quad (\text{A5})$$

where the terms  $\mathcal{Q}^{(n)}$  contain spectra of various orders and can be expressed as follows

$$\mathcal{Q}^{(n)} = \sum_{m=1}^{\infty} \frac{1}{m!} \sum_{\substack{n_1, \dots, n_m \geq 1 \\ n_1 + \dots + n_m = n}} \frac{1}{(n_1 + 2)! \cdots (n_m + 2)!} \times \sum_{\mathbf{k}_1^{(1)}, \dots, \mathbf{k}_{n_1+2}^{(1)}} \cdots \sum_{\mathbf{k}_1^{(m)}, \dots, \mathbf{k}_{n_m+2}^{(m)}} p^{(n_1+2)} \cdots p^{(n_m+2)} \times H_{\mathbf{k}_1^{(1)} \dots \mathbf{k}_{n_1+2}^{(1)} \dots \mathbf{k}_1^{(m)} \dots \mathbf{k}_{n_m+2}^{(m)}}, \quad (\text{A6})$$

with  $H$  standing for a generalization of the Hermite polynomials,

$$H_{\mathbf{k}_1 \dots \mathbf{k}_n} = \frac{(-1)^n}{\mathcal{P}_G[\alpha_{\mathbf{k}}]} \frac{\partial}{\partial \alpha_{\mathbf{k}_1}} \cdots \frac{\partial}{\partial \alpha_{\mathbf{k}_n}} \mathcal{P}_G[\alpha_{\mathbf{k}}]. \quad (\text{A7})$$

In our Universe structure formation roughly follows the hierarchical model, meaning we have that  $P^{(N)} \sim \mathcal{O}[P(k)^{N-1}]$ ,

such that any given term in the series expansion above is of the order

$$\mathcal{Q}^{(n)} \sim \varepsilon^{N-2}, \quad \varepsilon \equiv \sqrt{\frac{P(k)}{V}}. \quad (\text{A8})$$

It follows that the expansion is only meaningful as long as this parameter  $\varepsilon$  remains small. Furthermore, this allows us to conveniently keep track of the order of each term by counting powers of  $1/\sqrt{V}$ .

As we are going to evaluate ensemble averages comprising amplitudes and/or phases of Fourier modes, it is useful to split our variables accordingly and write them as  $\alpha_{\mathbf{k}} = A_{\mathbf{k}} e^{i\theta_{\mathbf{k}}}$ . However, due to the reality constraint,  $\alpha_{\mathbf{k}}$  and  $\alpha_{\mathbf{k}}^* = \alpha_{-\mathbf{k}}$  are not entirely independent from each other, which is why we restrict all summations over wavevectors to the upper half sphere (uhs), defined by  $k_z \geq 0$ . In this subspace the probability for a set of modes to take values within an infinitesimal interval is thus given by

$$\mathcal{P}(\{\alpha_{\mathbf{k}}, \alpha_{\mathbf{k}}^*\}) \prod_{\mathbf{k} \in \text{uhs}} d\alpha_{\mathbf{k}} d\alpha_{\mathbf{k}}^* = \mathcal{P}(\{A_{\mathbf{k}}, \theta_{\mathbf{k}}\}) \prod_{\mathbf{k} \in \text{uhs}} 2A_{\mathbf{k}} dA_{\mathbf{k}} d\theta_{\mathbf{k}}, \quad (\text{A9})$$

where the factor  $2A_{\mathbf{k}}$  comes from the Jacobian of the transformation. Expressing the  $\mathcal{Q}^{(n)}$  in terms of  $A_{\mathbf{k}}$  and  $\theta_{\mathbf{k}}$ , all resulting terms can be rearranged to display a similar structure:

$$\sum_{\substack{\mathbf{k}_1, \dots, \mathbf{k}_n \in \text{uhs} \\ \mathbf{k}_i \neq \mathbf{k}_j}} A_{\mathbf{k}_1} A_{\mathbf{k}_2} \cdots \cos(\theta_{\mathbf{k}_1} \pm \theta_{\mathbf{k}_2} \pm \cdots) \times p^{(n_1)}(\mathbf{k}_1, \dots, \mathbf{k}_{n_1}) p^{(n_2)}(\mathbf{k}_{n_1+1}, \dots, \mathbf{k}_{n_1+n_2}) \cdots, \quad (\text{A10})$$

and it is important to note that when integrating over the phases, we always get a vanishing result unless the cosine-term is cancelled by some means. That is only possible if we correlate a number of phase factors, which exactly matches the number of phases appearing in Eq. (A10). Since all other terms in Eq. (A6) give no contribution, this drastically simplifies our task of computing any particular phase correlator. From this observation also follows that any even (odd) phase correlator can only get contributions from even (odd)  $N$ -th order spectra. We will now consider some special cases, which occur in the main part of this work.

### A1 Four-point phase correlator

We only take into account terms of the order  $1/V$ , which corresponds to  $n = 2$  in the PDF expansion of Eq. (A5). After splitting each summation into separate sums over mutually different modes, we obtain the following two terms with four different phase factors,

$$\mathcal{Q}_1^{(2)} = \frac{1}{3} \sum_{\substack{\mathbf{k}_1, \mathbf{k}_2, \mathbf{k}_3 \\ \mathbf{k}_i \neq \mathbf{k}_j}}^{\text{uhs}} A_{\mathbf{k}_1} A_{\mathbf{k}_2} A_{\mathbf{k}_3} A_{\mathbf{k}_{123}} \times \cos(\theta_{\mathbf{k}_1} + \theta_{\mathbf{k}_2} + \theta_{\mathbf{k}_3} - \theta_{\mathbf{k}_{123}}) p^{(4)}(\mathbf{k}_1, \mathbf{k}_2, \mathbf{k}_3, -\mathbf{k}_{123}), \quad (\text{A11})$$

$$\begin{aligned} \mathcal{Q}_2^{(2)} &= \sum_{\substack{\text{uhs} \\ \mathbf{k}_1, \mathbf{k}_2, \mathbf{k}_3 \\ \mathbf{k}_i \neq \mathbf{k}_j}} A_{\mathbf{k}_1} A_{\mathbf{k}_2} A_{\mathbf{k}_3} A_{\mathbf{k}_{123}} \\ &\times \cos(\theta_{\mathbf{k}_1} + \theta_{\mathbf{k}_2} - \theta_{\mathbf{k}_3} - \theta_{\mathbf{k}_{123}}) p^{(4)}(\mathbf{k}_1, \mathbf{k}_2, -\mathbf{k}_3, -\mathbf{k}_{123}), \end{aligned} \quad (\text{A12})$$

where  $\mathbf{k}_{123} \equiv \mathbf{k}_1 + \mathbf{k}_2 + \mathbf{k}_3$ . We can trivially integrate over all amplitudes  $A_{\mathbf{k}}$  and by making use of the identity

$$\mathcal{I}(n) = \int_0^\infty A^n 2A e^{-A^2} dA = \Gamma\left(1 + \frac{n}{2}\right), \quad (\text{A13})$$

we see that both expressions above acquire a factor of  $\mathcal{I}(1)^4 = (\sqrt{\pi}/2)^4$  (note that  $\mathcal{I}(0) = 1$ ). Let us now consider the correlator  $\langle \epsilon_{\mathbf{q}_1} \epsilon_{\mathbf{q}_2} \epsilon_{\mathbf{q}_3} \epsilon_{-\mathbf{q}_{123}} \rangle$  with  $\mathbf{q}_1, \mathbf{q}_2, \mathbf{q}_3$  all in the upper half sphere, such that a contribution from Eq. (A11) looks as follows:

$$\begin{aligned} &\propto \sum_{\substack{\text{uhs} \\ \mathbf{k}_1, \mathbf{k}_2, \mathbf{k}_3 \\ \mathbf{k}_i \neq \mathbf{k}_j}} p^{(4)}(\mathbf{k}_1, \mathbf{k}_2, \mathbf{k}_3, -\mathbf{k}_{123}) \\ &\times \int \frac{d\theta_{\mathbf{q}_1}}{2\pi} e^{i\theta_{\mathbf{q}_1}} \int \frac{d\theta_{\mathbf{q}_2}}{2\pi} e^{i\theta_{\mathbf{q}_2}} \int \frac{d\theta_{\mathbf{q}_3}}{2\pi} e^{i\theta_{\mathbf{q}_3}} \int \frac{d\theta_{\mathbf{q}_{123}}}{2\pi} e^{-i\theta_{\mathbf{q}_{123}}} \\ &\times \prod_{\mathbf{p} \neq \mathbf{q}_i}^{\text{uhs}} \int \frac{d\theta_{\mathbf{p}}}{2\pi} \cos(\theta_{\mathbf{k}_1} + \theta_{\mathbf{k}_2} + \theta_{\mathbf{k}_3} - \theta_{\mathbf{k}_{123}}). \end{aligned} \quad (\text{A14})$$

As was already mentioned above, unless all phase factors are cancelled, the whole expression will evaluate to zero. Non-zero contributions therefore stem from cases where each  $\mathbf{q}$ -mode equals one of the  $\mathbf{k}$ -modes, giving in total  $3! = 6$  different permutations. Eq. (A12) does not add to this exemplary configuration and the full result is hence

$$\langle \epsilon_{\mathbf{q}_1} \epsilon_{\mathbf{q}_2} \epsilon_{\mathbf{q}_3} \epsilon_{-\mathbf{q}_{123}} \rangle = \left(\frac{\sqrt{\pi}}{2}\right)^4 p^{(4)}(\mathbf{q}_1, \mathbf{q}_2, \mathbf{q}_3, -\mathbf{q}_{123}). \quad (\text{A15})$$

It can be checked that this holds true for all possible configurations of the  $\mathbf{q}$ -modes.

## A2 Six-point phase correlator

The lowest order contributions to the connected six-point phase correlator come from terms with  $n = 4$  in the PDF expansion. In this case we find three terms with six different phase factors,

$$\begin{aligned} \mathcal{Q}_1^{(4)} &= \frac{1}{60} \sum_{\substack{\text{uhs} \\ \mathbf{k}_1, \dots, \mathbf{k}_5 \\ \mathbf{k}_i \neq \mathbf{k}_j}} A_{\mathbf{k}_1} \cdots A_{\mathbf{k}_5} A_{\mathbf{k}_{12345}} \\ &\times \cos(\theta_{\mathbf{k}_1} + \theta_{\mathbf{k}_2} + \theta_{\mathbf{k}_3} + \theta_{\mathbf{k}_4} + \theta_{\mathbf{k}_5} - \theta_{\mathbf{k}_{12345}}) \\ &\times p^{(6)}(\mathbf{k}_1, \mathbf{k}_2, \mathbf{k}_3, \mathbf{k}_4, \mathbf{k}_5, -\mathbf{k}_{12345}), \end{aligned} \quad (\text{A16})$$

$$\begin{aligned} \mathcal{Q}_2^{(4)} &= \frac{1}{24} \sum_{\substack{\text{uhs} \\ \mathbf{k}_1, \dots, \mathbf{k}_5 \\ \mathbf{k}_i \neq \mathbf{k}_j}} A_{\mathbf{k}_1} \cdots A_{\mathbf{k}_5} A_{\mathbf{k}_{12345}} \\ &\times \cos(\theta_{\mathbf{k}_1} + \theta_{\mathbf{k}_2} + \theta_{\mathbf{k}_3} + \theta_{\mathbf{k}_4} - \theta_{\mathbf{k}_5} - \theta_{\mathbf{k}_{12345}}) \\ &\times p^{(6)}(\mathbf{k}_1, \mathbf{k}_2, \mathbf{k}_3, \mathbf{k}_4, -\mathbf{k}_5, -\mathbf{k}_{12345}), \end{aligned} \quad (\text{A17})$$

$$\begin{aligned} \mathcal{Q}_3^{(4)} &= \frac{1}{36} \sum_{\substack{\text{uhs} \\ \mathbf{k}_1, \dots, \mathbf{k}_5 \\ \mathbf{k}_i \neq \mathbf{k}_j}} A_{\mathbf{k}_1} \cdots A_{\mathbf{k}_5} A_{\mathbf{k}_{12345}} \\ &\times \cos(\theta_{\mathbf{k}_1} + \theta_{\mathbf{k}_2} + \theta_{\mathbf{k}_3} - \theta_{\mathbf{k}_4} - \theta_{\mathbf{k}_5} - \theta_{\mathbf{k}_{12345}}) \\ &\times p^{(6)}(\mathbf{k}_1, \mathbf{k}_2, \mathbf{k}_3, -\mathbf{k}_4, -\mathbf{k}_5, -\mathbf{k}_{12345}), \end{aligned} \quad (\text{A18})$$

As for the the four-point phase correlator we first integrate out all amplitudes, which now gives rise to a factor  $(\sqrt{\pi}/2)^6$  each, where we have made use of Eq. (A13) again. We then consider a six-point correlator of the form  $\langle \epsilon_{\mathbf{q}_1} \epsilon_{\mathbf{q}_2} \epsilon_{-\mathbf{q}_{12}} \epsilon_{\mathbf{q}'_1} \epsilon_{\mathbf{q}'_2} \epsilon_{-\mathbf{q}'_{12}} \rangle$  and assume that  $\mathbf{q}_1, \mathbf{q}_2, \mathbf{q}'_1, \mathbf{q}'_2 \in \text{uhs}$ . In this case only Eq. (A17) can give a non-vanishing contribution and for that  $\mathbf{q}_{12}$  and  $\mathbf{q}'_{12}$  must equal either  $\mathbf{k}_5$  or  $\mathbf{k}_{12345}$  and all other  $\mathbf{q}$ - and  $\mathbf{q}'$ -modes must be identified with the remaining  $\mathbf{k}$ -modes. This gives  $2 \times 4! = 48$  possibilities and thus we get

$$\begin{aligned} &\langle \epsilon_{\mathbf{q}_1} \epsilon_{\mathbf{q}_2} \epsilon_{-\mathbf{q}_{12}} \epsilon_{\mathbf{q}'_1} \epsilon_{\mathbf{q}'_2} \epsilon_{-\mathbf{q}'_{12}} \rangle \\ &= \left(\frac{\sqrt{\pi}}{2}\right)^6 p^{(6)}(\mathbf{q}_1, \mathbf{q}_2, -\mathbf{q}_{12}, \mathbf{q}'_1, \mathbf{q}'_2, -\mathbf{q}'_{12}), \end{aligned} \quad (\text{A19})$$

which is also valid for any configuration of the six modes.

## A3 Mixed five-point correlator

Finally, we have to consider the mixed five-point correlator between five phases and two amplitudes, whose leading contributions are of the order  $1/V^{3/2}$ , i.e.  $n = 3$ . There are two terms in the Edgeworth expansion, which have five different phase factors:

$$\begin{aligned} \mathcal{Q}_1^{(3)} &= \frac{1}{12} \sum_{\substack{\text{uhs} \\ \mathbf{k}_1, \dots, \mathbf{k}_4 \\ \mathbf{k}_i \neq \mathbf{k}_j}} A_{\mathbf{k}_1} \cdots A_{\mathbf{k}_4} A_{\mathbf{k}_{1234}} \\ &\times \cos(\theta_{\mathbf{k}_1} + \theta_{\mathbf{k}_2} + \theta_{\mathbf{k}_3} + \theta_{\mathbf{k}_4} - \theta_{\mathbf{k}_{1234}}) \\ &\times p^{(5)}(\mathbf{k}_1, \mathbf{k}_2, \mathbf{k}_3, \mathbf{k}_4, -\mathbf{k}_{1234}), \end{aligned} \quad (\text{A20})$$

$$\begin{aligned} \mathcal{Q}_2^{(3)} &= \frac{1}{6} \sum_{\substack{\text{uhs} \\ \mathbf{k}_1, \dots, \mathbf{k}_4 \\ \mathbf{k}_i \neq \mathbf{k}_j}} A_{\mathbf{k}_1} \cdots A_{\mathbf{k}_4} A_{\mathbf{k}_{1234}} \\ &\times \cos(\theta_{\mathbf{k}_1} + \theta_{\mathbf{k}_2} + \theta_{\mathbf{k}_3} - \theta_{\mathbf{k}_4} - \theta_{\mathbf{k}_{1234}}) \\ &\times p^{(5)}(\mathbf{k}_1, \mathbf{k}_2, \mathbf{k}_3, -\mathbf{k}_4, -\mathbf{k}_{1234}), \end{aligned} \quad (\text{A21})$$

Let us consider the correlator  $\langle \delta_{\mathbf{k}_1} \delta_{\mathbf{k}_2} \epsilon_{\mathbf{q}_1} \epsilon_{\mathbf{q}_2} \epsilon_{\mathbf{q}_3} \rangle$ , where we assume that  $\mathbf{k}_1, \mathbf{k}_2, \mathbf{q}_1, \mathbf{q}_2 \in \text{uhs}$  and  $\mathbf{q}_3 \in \text{lhs}$ . All terms involving  $\mathcal{Q}_2^{(3)}$  will evaluate to zero and from the amplitude integrals we obtain a factor  $\mathcal{I}(1)^3 \times \mathcal{I}(2)^2 = (\sqrt{\pi}/2)^3$ . We are thus left with the following phase integrals:

$$\begin{aligned} \langle \delta_{\mathbf{k}_1} \delta_{\mathbf{k}_2} \epsilon_{\mathbf{q}_1} \epsilon_{\mathbf{q}_2} \epsilon_{\mathbf{q}_3} \rangle &= \sqrt{P(k_1) P(k_2)} \left(\frac{\sqrt{\pi}}{2}\right)^3 \frac{V}{12} \int \prod_{\mathbf{p} \in \text{uhs}} \frac{d\theta_{\mathbf{p}}}{2\pi} \\ &\times \sum_{\substack{\mathbf{u}_1, \dots, \mathbf{u}_4 \in \text{uhs} \\ \mathbf{u}_i \neq \mathbf{u}_j}} \cos(\theta_{\mathbf{u}_1} + \cdots + \theta_{\mathbf{u}_4} - \theta_{\mathbf{u}_{1234}}) \\ &\times p^{(5)}(\mathbf{u}_1, \dots, -\mathbf{u}_{1234}) e^{i(\theta_{\mathbf{k}_1} + \theta_{\mathbf{k}_2} + \theta_{\mathbf{q}_1} + \theta_{\mathbf{q}_2} - \theta_{\mathbf{q}_3})}, \end{aligned} \quad (\text{A22})$$

which only give a non-vanishing result if we impose the condition that  $\mathbf{q}_3 = -\mathbf{k}_1 - \mathbf{k}_2 - \mathbf{q}_1 - \mathbf{q}_2$ . We then have  $4! = 24$

possibilities of matching the various  $\mathbf{k}$ - and  $\mathbf{q}$ -modes with the  $\mathbf{u}$ -vectors and after taking the continuum limit we finally get:

$$\begin{aligned} \langle \delta_{\mathbf{k}_1} \delta_{\mathbf{k}_2} \epsilon_{\mathbf{q}_1} \epsilon_{\mathbf{q}_2} \epsilon_{\mathbf{q}_3} \rangle &= (2\pi)^3 \left( \frac{\sqrt{\pi}}{2} \right)^3 \sqrt{P(k_1) P(k_2)} \\ &\times p^{(5)}(\mathbf{k}_1, \mathbf{k}_2, \mathbf{q}_1, \mathbf{q}_2, \mathbf{q}_3) \\ &\times \delta_D(\mathbf{k}_1 + \mathbf{k}_2 + \mathbf{q}_1 + \mathbf{q}_2 + \mathbf{q}_3). \end{aligned} \quad (\text{A23})$$

As before this result is not restricted to the particular configuration of wavevectors we have chosen above.

## APPENDIX B: GALAXY POWER SPECTRUM AT ONE-LOOP ORDER

At linear order the power spectrum is only dependent on the single bias parameter  $b_1$ , while at the one-loop level non-linear and non-local bias introduce some additional terms that we need to account for. The full galaxy power spectrum at one-loop order is therefore given by (McDonald & Roy 2009):

$$\begin{aligned} P_g(k) &= b_1^2 P(k) + 2b_2 b_1 P_{b_2}(k) + 2b_{s^2} b_1 P_{b_{s^2}}(k) \\ &+ b_2^2 P_{b_{22}}(k) + 2b_2 b_{s^2} P_{b_2, b_{s^2}}(k) + b_{s^2}^2 P_{b_{s^2 22}}(k) \\ &+ 2b_1 b_{3nl} \sigma_3^2(k) P_L(k), \end{aligned} \quad (\text{B1})$$

where  $P(k)$  and  $P_L(k)$  denote the one-loop and linear dark matter power spectra, respectively. The power spectra that appear in combination with the bias parameters  $b_2$  and  $b_{s^2}$  are given by the following integrals,

$$P_{b_2}(k) = \int \frac{d^3 q}{(2\pi)^3} P_L(q) P_L(|\mathbf{k} - \mathbf{q}|) F_2(\mathbf{q}, \mathbf{k} - \mathbf{q}), \quad (\text{B2})$$

$$\begin{aligned} P_{b_{s^2}}(k) &= \int \frac{d^3 q}{(2\pi)^3} P_L(q) P_L(|\mathbf{k} - \mathbf{q}|) F_2(\mathbf{q}, \mathbf{k} - \mathbf{q}) \\ &\times S_2(\mathbf{q}, \mathbf{k} - \mathbf{q}), \end{aligned} \quad (\text{B3})$$

$$\begin{aligned} P_{b_2, b_{s^2}}(k) &= -\frac{1}{2} \int \frac{d^3 q}{(2\pi)^3} P_L(q) \left[ \frac{2}{3} P_L(q) \right. \\ &\left. - P_L(|\mathbf{k} - \mathbf{q}|) S_2(\mathbf{q}, \mathbf{k} - \mathbf{q}) \right], \end{aligned} \quad (\text{B4})$$

$$\begin{aligned} P_{b_{s^2 22}}(k) &= -\frac{1}{2} \int \frac{d^3 q}{(2\pi)^3} P_L(q) \left[ \frac{4}{9} P_L(q) \right. \\ &\left. - P_L(|\mathbf{k} - \mathbf{q}|) S_2(\mathbf{q}, \mathbf{k} - \mathbf{q})^2 \right], \end{aligned} \quad (\text{B5})$$

$$P_{b_{22}}(k) = -\frac{1}{2} \int \frac{d^3 q}{(2\pi)^3} P_L(q) [P_L(q) - P_L(|\mathbf{k} - \mathbf{q}|)], \quad (\text{B6})$$

$$\begin{aligned} \sigma_3^2(k) &= -\frac{1}{2} \int \frac{d^3 q}{(2\pi)^3} P_L(q) \left[ \frac{5}{6} + \frac{15}{8} S_2(\mathbf{q}, \mathbf{k} - \mathbf{q}) S_2(-\mathbf{q}, \mathbf{k}) \right. \\ &\left. - \frac{5}{4} S_2(\mathbf{q}, \mathbf{k} - \mathbf{q}) \right], \end{aligned} \quad (\text{B7})$$

where the kernel functions  $F_2$  and  $S_2$  are defined in Eqs. (11) and (15). Assuming that galaxy bias is local in Lagrangian space, the non-local terms can be related at first order to the linear bias term as follows (Baldauf et al. 2012; Chan et al. 2012; Saito et al. 2014):

$$b_{s^2} = -\frac{4}{7} (b_1 - 1), \quad (\text{B8})$$

$$b_{3nl} = \frac{32}{315} (b_1 - 1). \quad (\text{B9})$$

This paper has been typeset from a  $\text{\TeX}/\text{\LaTeX}$  file prepared by the author.